

A multi-wavelength analysis of the diffuse H II region G25.8700+0.1350

S. Cichowolski^{1*}, N. U. Duronea^{2*}, L. A. Suad^{2*}, E. M. Reynoso^{1*}, R. Dorda³

¹ Instituto de Astronomía y Física del Espacio (UBA, CONICET), CC 67, Suc. 28, 1428 Buenos Aires, Argentina

² Instituto Argentino de Radioastronomía (CCT-La Plata, CONICET; CICPBA), C.C. No. 5, 1894, Villa Elisa, Argentina

³ Departamento de Física, Ingeniería de Sistemas y Teoría de la Señal, Universidad de Alicante, Carretera de San Vicente del Raspeig, E03690 Alicante, Spain

ABSTRACT

We present a multiwavelength investigation of the H II region G25.8700+0.1350, located in the inner part of the Galaxy. In radio continuum emission, the region is seen as a bright arc-shaped structure. An analysis of the H I line suggests that G25.8700+0.1350 lies at a distance of 6.5 kpc. The ionized gas is bordered by a photodissociation region which is encircled by a molecular structure where four molecular clumps are detected. At infrared wavelengths, the region is also very conspicuous. Given the high level of visual absorption in the region, the exciting stars should be searched for in the infrared band. In this context, we found in the literature one Wolf-Rayet and one red supergiant which, together with 37 2MASS sources candidates to be O-type stars, could be related to the origin of G25.8700+0.1350. Finally, as expanding H II regions are hypothesized to trigger star formation, we used different infrared point source catalogues to search for young stellar object candidates (cYSOs). A total of 45 cYSOs were identified projected onto the molecular clouds.

Key words: Stars: massive - ISM: bubbles - H II regions - Infrared: ISM - Stars: formation

1 INTRODUCTION

Massive stars are known to play an important role in disrupting, modifying, and dispersing the ambient molecular gas through their ultraviolet (UV) radiation, strong winds, outflows, and eventually, with supernova explosions. The strong UV radiation of massive stars, ionizes the molecular gas creating H II regions, which are expected to expand in the interstellar medium because of the high difference in pressure between the ionized and the ambient neutral gas. This can originate large distortions in their surroundings and even compression of nearby molecular clouds stimulating the formation of a new generation of stars (Elmegreen & Lada 1977; Lefloch & Lazareff 1994; Zinnecker & Yorke 2007).

The feedback of massive stars and the evolution of their associated H II regions determine the physical conditions of their environs and the star formation rate in the region. Hence, it is important to study the interstellar medium adjacent to Galactic H II regions since they can provide substantial information, not only about the physical conditions where massive stars are born, but also to set empirical constraints to existing theoretical models and to improve our knowledge of the physical processes leading to stellar formation and evolution.

In this paper we present the very first multiwavelength analysis of the diffuse H II region catalogued by Helfand et al. (2006)

as G25.8700+0.1350. This region consists in a large, bright partial arc, located in the inner Galaxy, near the tangent point as inferred from observations in several radio recombination lines (RRL). This H II region is especially interesting because it is close to two young high-mass clusters, RSGC1 (Figer et al. 2006; Davies et al. 2008) and RSGC2 (Davies et al. 2007), which are dominated by red supergiants (RSGs), evolved high-mass stars. These clusters are separated from the center of G25.8700+0.1350 by 39'8 and 22'6 respectively. Moreover, the largest concentration of red supergiants (RSGs) known in our Galaxy (Negueruela et al. 2012; Dorda et al. 2016) can be found around these clusters. According to the high density of RSGs, this region probably is one of the most intense star-forming places in the Galaxy.

2 DATA SETS

To carry out this study we made use of public archival data from near-IR to radio wavelengths. In what follows, we describe the datasets employed.

- Radio continuum data at 1420 MHz were extracted from the Multi-Array Galactic Plane Imaging Survey (MAGPIS; Helfand et al. 2006). This survey was constructed combining Very Large Array (VLA) observations in the B, C, and D arrays. VLA data have a limited u, v coverage, and are insensitive to structures much larger than 1 arcmin. Hence, the MAGPIS images include short spatial frequencies obtained from observations with

* Member of the Carrera del Investigador Científico of CONICET, Argentina.

the 100-m Effelsberg radiotelescope so as to sample all diffuse, extended structures. The angular resolution is $6''.2 \times 5''.4$, and the sensitivity, $0.2 \text{ mJy beam}^{-1}$.

- IR data were obtained from the Herschel infrared Galactic Plane Survey (Hi-Gal). Hi-Gal (Molinari et al. 2010) used the Photodetector Array Camera and Spectrometer (PACS; Poglitsch et al. 2010) and the Spectral and Photometric Imaging Receiver (SPIRE; Griffin et al. 2010) cameras. The instruments detecting emission at 70 , $160 \mu\text{m}$ (PACS) and $250 \mu\text{m}$ (SPIRE) have angular resolutions of $5''.5$, $12''$, and $17''$, respectively. We obtained the UNIMAP level 2.5 images using the Herschel Science Archive.¹ We complemented IR emission using data from the Spitzer Space Telescope. We used the emission at $8 \mu\text{m}$ from the Infrared Array Camera (IRAC; Werner et al. 2004), and $24 \mu\text{m}$ from the Multiband Imaging Photometer (MIPS; Rieke et al. 2004). The spatial resolutions are $2''$ and $6''$ for 8 and $24 \mu\text{m}$, respectively.

- We used H I 21 cm data from the VLA Galactic Plane Survey (VGPS; Stil et al. 2006). As in the case of MAGPIS, the interferometric data must be completed with short-spacings to sample extended structures. In this survey, single dish data were supplied by the Green Bank Telescope (GBT). The H I line data of the VGPS have an angular resolution of $1' \times 1'$ and a spectral resolution of 1.56 km s^{-1} , although channels are sampled each 0.824 km^{-1} for consistency with the Canadian Galactic Plane Survey (CGPS).

- To survey the molecular emission, we used $^{13}\text{CO}(1-0)$ line data obtained from the Boston University-FCRAO Galactic Ring Survey (GRS²; Jackson et al. 2006) carried out with the SEQUOIA multi-pixel array receiver on the FCRAO 14 m telescope. This survey covers the Galactic plane in the range $18^\circ 0' < l < 55^\circ 7'$ and $-1^\circ 0' < b < 1^\circ 0'$, and has a sensitivity $< 0.4 \text{ K}$. The angular resolution and sampling are $46''$ and $22''$, respectively. The velocity resolution is 0.2 km s^{-1} , covering a range from -5 km s^{-1} to $+135 \text{ km s}^{-1}$, respectively. We also used CO(3-2) line data obtained from the CO High-Resolution Survey (COHRS³; Dempsey, Thomas & Currie 2013). The data were taken using the Heterodyne Array Receiver Programme on the James Clerk Maxwell Telescope (JCMT). The angular resolution and sampling are $14''$ and $6''$, respectively. The velocity resolution is 1 km s^{-1} , spanning from -30 km s^{-1} to $+155 \text{ km s}^{-1}$, respectively.

- We used 1.1 mm continuum data from the Bolocam Galactic Plane Survey (BGPS)⁴. This survey is contiguous over the range $-10^\circ 5' \leq l \leq 90^\circ 5'$, $|b| \leq 0^\circ 5'$, and is extended to $|b| \leq 1^\circ 5'$ for $75^\circ 5' \leq l \leq 87^\circ 5'$. Additional cross-cuts were performed at $l = 3^\circ 0'$, $15^\circ 0'$, $30^\circ 0'$, and $31^\circ 0'$, and four supplementary regions of the outer Galaxy, covering 170 deg^2 in total (Aguirre et al. 2011). Bolocam is a facility consisting of a 144-element bolometer array camera mounted at the Cassegrain focus of the 10.4 m mirror of the CSO on the summit of Mauna Kea. The array field of view (FOV) of the instrument is $7'.5$, and its effective resolution is $33''$ (Glenn et al. 2003).

3 G25.8700+0.1350 AND ITS LOCAL ISM

Figure 1 shows the emission distribution of the region under study at 1420 MHz . G25.8700+0.1350 is the large, bright source, whose location and size, as given by Helfand et al. (2006), are indicated by the box. Several RRLs were detected in the region (see Fig. 1). Lockman, Pisano & Howard (1996) detected the 6 cm (H109 α and H111 α) RRL at $(l, b) = (25^\circ 945', +0^\circ 125')$ at the velocity of $104.0 \pm 1.1 \text{ km s}^{-1}$. The line $110 \text{ H}\alpha$ was detected at $(l, b) = (25^\circ 8', +0^\circ 24')$ at the velocity of $112.1 \pm 0.1 \text{ km s}^{-1}$ by Sewilo et al. (2004). Finally, Quireza et al. (2006a) detected towards $(l, b) = (25^\circ 766', +0^\circ 212')$, the 91α and 92α lines of the H, He and C at $111.44 \pm 0.17 \text{ km s}^{-1}$, $111.35 \pm 1.89 \text{ km s}^{-1}$ and $124.52 \pm 0.96 \text{ km s}^{-1}$, respectively.

Since G25.8700+0.1350 is located in the first Galactic quadrant, two distances, near (N) and far (F), are possible for each radial velocity up to the tangent point. Resolving the kinematic distance ambiguity (KDA) is not easy, specially when the radial velocity of the source is very close to the velocity of the tangent point (T). The most straightforward method to solve the KDA for H II regions consists in constructing a 21 cm H I absorption spectrum toward the radio continuum emission and compare the absorption features with corresponding H I emission peaks, where the last emission feature detected indicates the velocity of the tangent point. The detection of H I absorption up to the tangent point implies that the source lies at the far distance inferred from the RRL velocity. Otherwise, it is safe to assume that the H II region is located at the near distance.

In the direction of G25.8700+0.1350, the velocity of the tangent point is about $+125 \text{ km s}^{-1}$, and the corresponding kinematic distance, around 7.7 kpc . Several attempts are found in the literature to solve for the KDA in G25.8700+0.1350. Applying the canonical method described above, Quireza et al. (2006b) inferred that the region is at 7.3 kpc , which corresponds to the near distance. On the other hand, Sewilo et al. (2004) used H_2CO line observations to disentangle the KDA problem for several H II regions; for G25.8700+0.1350, they cannot unambiguously distinguish between the near and far position. Finally, Anderson & Bania (2009) resolved the KDA using H I and ^{13}CO surveys for 266 H II regions located in the inner Galaxy with RRL emission detected and with molecular gas associated (Anderson et al. 2009). In addition to performing the usual absorption analysis, they searched for self-absorption by comparing the H I and ^{13}CO lines, where the signature of self-absorption is the presence of an H I absorption feature together with molecular emission at the same velocity.

In Table 1, we summarize the relevant results reported by Anderson & Bania (2009). In the area of G25.8700+0.1350 the authors identified five molecular clouds related to ionized gas, which are indicated by grey ellipses in Fig. 1 and described in Table 1. Column 2 gives the ID of the H II regions related to each cloud as given by Anderson et al. (2009), while their Galactic coordinates are given in columns 3 and 4. Column 5 gives the radial velocity of the detected RRL. Columns 6 and 8 show the result (N, F, T) obtained according to each method, either the conventional H I absorption analysis (dubbed 'EA' for Emission/Absorption) or the search for self-absorption ('SA'). Columns 7 and 9 give their corresponding quality parameters, where 'A' and 'B' stand, respectively, for high and low confidence of the results. Finally, the suggested distance is given in column 10. As can be seen in Fig. 1, clouds 1 and 2 are related to another H II region (cataloged as G25.7056+0.0389 by Helfand et al. 2006), while clouds 3, 4, and 5 are probably associated with G25.8700+0.1350 since they share both the radial velocity and spatial location. It calls the attention,

¹ <http://www.cosmos.esa.int/web/herschel/science-archive>

² http://www.bu.edu/galacticring/new_index.htm

³ <http://dx.doi.org/10.11570/13.0002>

⁴ <http://irsa.ipac.caltech.edu/Missions/bolocam.html>

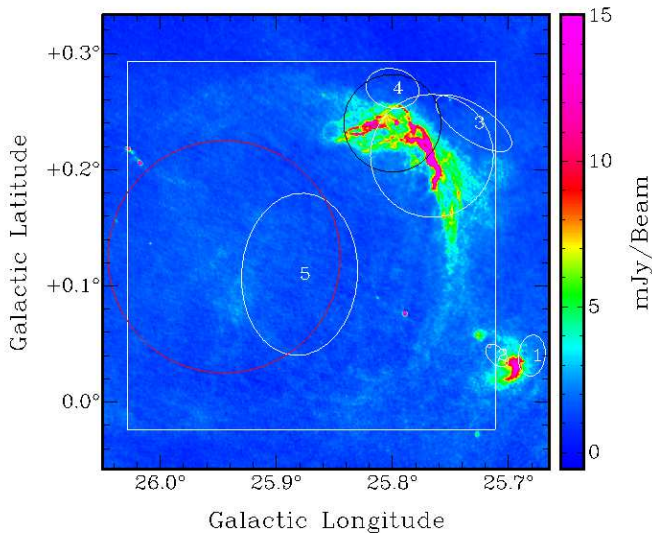


Figure 1. Radio continuum image of the region at 1420 MHz obtained from MAGPIS. The box indicates the location of G25.8700+0.1350. Red, black, and white circles indicate the locations where RRL were detected by Lockman, Pisano & Howard (1996), Sewilo et al. (2004), and Quireza et al. (2006a) respectively. The size of the circles correspond to the beam size of each observation. The ellipses, numbered as in Table 1, enclose the ionized regions having CO associated, as indicated by Anderson & Bania (2009).

however, that while regions 3 and 4 are put at the near distance, region 5 seems to be, although with less reliability, at the far side.

In summary, even though the distance to G25.8700+0.1350 has been estimated by many authors, there is no agreement in the different results they achieve. Since having an accurate distance is crucial for determining the physical properties of the region, we will obtain our own estimation based on the radio continuum and H I available data.

3.1 Distance estimation

In what follows, we perform an H I absorption study of G25.8700+0.1350 with the aim of constraining its systemic velocity and distance. For consistency, we have convolved the 1420 MHz continuum image obtained from MAGPIS down to the resolution of the H I data. The on-source (T_{on}) absorption profile was obtained towards the brightest region of G25.8700+0.1350, enclosed by the radio continuum isophote at $600 \text{ mJy beam}^{-1}$. To obtain the expected H I profile at this region (T_{off}), we performed a bilinear fit using only the H I pixels within the yellow box in Fig. 2 outside the outer radio continuum contour, at $350 \text{ mJy beam}^{-1}$. The method (e.g. Reynoso, Cichowolski & Walsh 2017) consists in replacing those pixels within the inner contour by the average between two linear fits: one along Galactic Latitude and the other along Galactic Longitude. The result is shown by the blue solid line in Fig. 3. The absorption feature at the highest positive value appears at $\sim +115 \text{ km s}^{-1}$. No absorption features are seen at negative values.

To facilitate the analysis of the H I absorption profile associated with G25.8700+0.1350, we followed the same method described above and obtained a second profile towards the bright, nearby H II region G25.7056+00389. The result is displayed by the red solid lines in Fig. 3. A comparison between both profiles readily shows that although the H I emission level at $\sim +125 \text{ km s}^{-1}$ is the same for both sources, the red absorption profile contains a $\sim 10 \text{ km}$

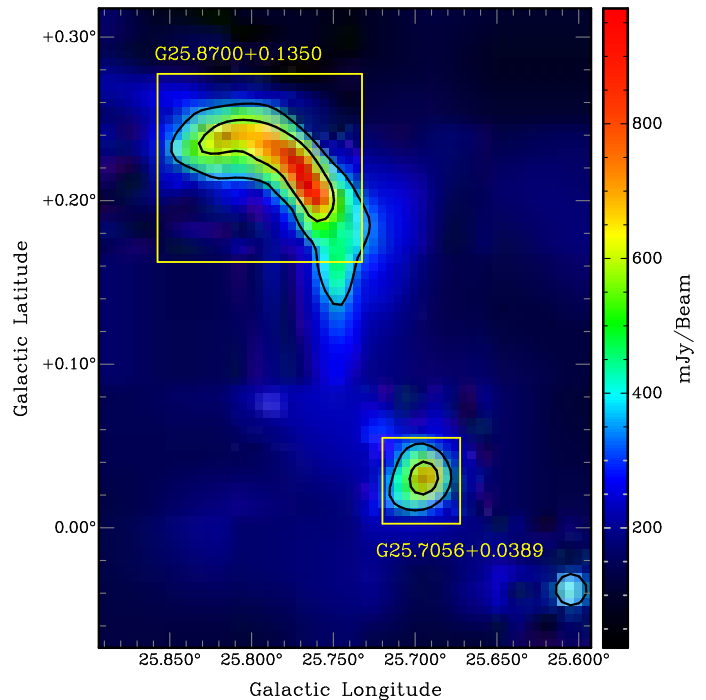


Figure 2. MAGPIS image of the region at 1420 MHz convolved to a $60' \times 60'$ beam in order to match the resolution of the H I data. The intensity scale is displayed by a color bar to the right. The two yellow boxes indicate the regions used to compute the absorption profiles towards G25.8700+0.1350 and G25.7056+00389, shown in Fig. 3. Black contours at 350 and $600 \text{ mJy beam}^{-1}$ are plotted.

s^{-1} -width feature which is absent in the blue profile. We thus interpret that the last absorption feature towards G25.8700+0.1350 occurs before reaching the tangent point, and hence the region lies in the near side of the two possible distances associated with $v = +115 \text{ km s}^{-1}$: 6.5 and 8.7 kpc, according to the Galactic rotation model of Fich, Blitz & Stark (1989). In what follows, we will adopt a distance of $6.5 \pm 1 \text{ kpc}$ for G25.8700+0.1350.

3.2 1420 MHz emission

3.2.1 Radio continuum

Figure 1 clearly shows that G25.8700+0.1350 presents a very bright arc-shape structure superposed onto a faint, more extended emission. We estimated the average flux density of this emission to be $1.3 \text{ mJy beam}^{-1}$. Accounting for this background, we obtained that the total flux density of the bright arc is $S_{1420} = 12 \pm 1 \text{ Jy}$, where the uncertainty involves any arbitrary assumption in determining the limits of the region.

We then estimate the physical parameters of G25.8700+0.1350 using the model developed by Mezger & Henderson (1967). We consider the spherical source model, with an angular diameter of $\theta_{\text{sph}} = 20'$ and a filling factor of 0.08. Assuming our estimated distance value $D = 6.5 \pm 1.0 \text{ kpc}$, and the electron temperature inferred by Quireza et al. (2006b), $T_e = 6120 \pm 100 \text{ K}$, we obtain that the region contains $2500 \pm 1110 M_{\odot}$ of hydrogen ionized mass and an electron density of $n_e = 43 \pm 10 \text{ cm}^{-3}$, which is similar to the value $n_e = 45.7 \text{ cm}^{-3}$ obtained by Quireza et al. (2006b) using RRL data.

Table 1. Parameters of H II regions associated with CO clouds.

	ID	l (deg.)	b (deg.)	V_{LSR} (km s $^{-1}$)	EA	Q-EA	SA	Q-SA	D (kpc)
1	U25.72+0.05a	25.72	0.05	53.3	–	–	N	B	3.6
2	U25.72+0.05b	25.72	0.05	102.0	–	–	F	A	9.2
3	C25.77+0.21	25.77	0.21	110.8	T	–	N	A	6.7
4	U25.80+0.24	25.80	0.24	112.1	T	–	N	A	6.8 ^a
5	D25.94+0.10	25.94	0.10	104.0	T	–	F	B	9.1

^a The distance information given for this source is confusing since its radial velocity was not properly taken from the work of Anderson et al. (2009). We adopt the near distance associated with $V_{\text{LSR}} = 112.1$ km s $^{-1}$ instead of the one given by Anderson & Bania (2009), i.e. 7.7 kpc.

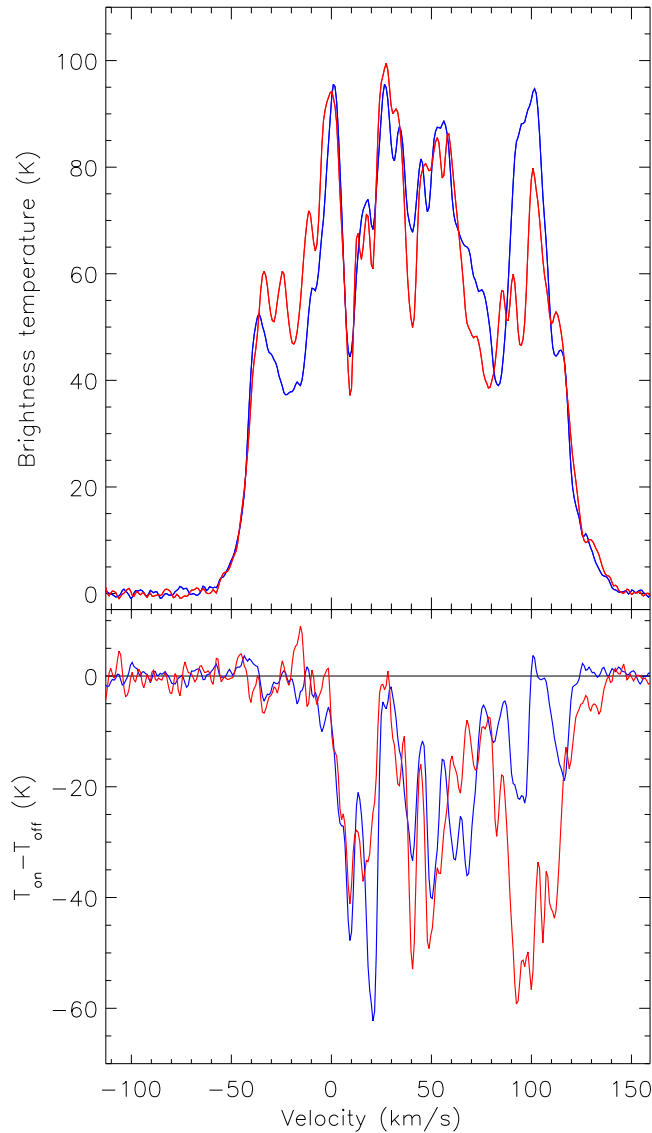


Figure 3. H I emission-absorption pairs towards G25.8700+0.1350 (blue lines) and G25.7056+00389 (red lines). Off-source H I profiles were computed employing a bilinear fit as explained in the text.

Finally, we can estimate the number of UV photons necessary to keep the gas ionized, using the relation

$$N_{\text{UV}} = 0.76 \times 10^{47} \left(\frac{T_e}{10^4 \text{K}} \right)^{-0.45} \left(\frac{v}{\text{GHz}} \right)^{0.1} \left(\frac{D}{\text{kpc}} \right)^2 \left(\frac{S_{\nu}}{Jy} \right) \text{s}^{-1} \text{ (Chaisson 1976), which yields } N_{\text{UV}} = (5.0 \pm 1.6) \times 10^{49} \text{ s}^{-1} \text{ for G25.8700+0.1350.}$$

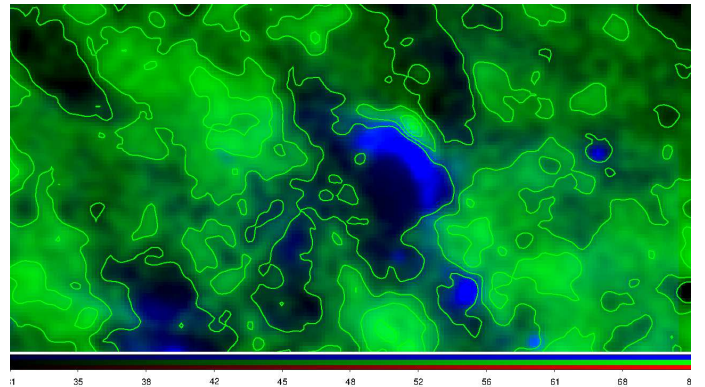


Figure 4. Green: H I emission distribution averaged in the velocity range from 109.8 to 118.1 km s $^{-1}$. Contour levels are at 40, 50, 60, and 70 K. Blue: radio continuum emission at 1420 MHz.

3.2.2 H I line emission distribution

We have inspected the H I emission distribution in the velocity range where the RRLs were observed and noticed two striking features in the velocity interval from 109.8 to 118.1 km s $^{-1}$ (Fig. 4): a) a conspicuous H I emission minimum around $(l, b) = (25^{\circ}8, 0^{\circ}2)$, and b) a bright H I feature observed next to the arc-shaped structure detected in the radio continuum emission at 1420 MHz (see Sect. 3.2.1). Both features strongly suggest that the massive stars have ionized and probably swept up the surrounding ionized and neutral gas, generating an irregular cavity (Weaver et al. 1977). The morphology of G25.8700+0.1350 could be explained then as an H II region bounded by density toward higher Galactic longitudes, and bounded by ionization toward lower Galactic longitudes, probably as a result of the action of the powering stars over an inhomogeneously distributed original neutral gas. This scenario is in agreement with the morphology of the molecular gas component reported in the velocity range from 106.6 to 116.6 km s $^{-1}$ toward higher Galactic longitudes, assumed to be related with the PDR (see Sect. 3.4). It is important to mention, however, that an inspection of all the H I emission channels show that there is no emission that could be interpreted as the approaching and receding caps. This absence may be indicating either that the structure has a ring morphology or, as pointed out by Cazzolato & Pineault (2005), that there is significant velocity dispersion, making the receding and/or expanding caps hard to detect.

3.3 Infrared

At infrared wavelengths, the region appears to be very conspicuous, as shown in Fig. 5. In fact, G25.8700+0.1350 was also iden-

tified in the WISE images and catalogued as G025.867+00.118 (Anderson et al. 2014). Figure 5 is a composite RGB image of the region, where the emission at $250 \mu\text{m}$, $24 \mu\text{m}$, and $8 \mu\text{m}$ is displayed in red, green, and blue respectively. Since the $8 \mu\text{m}$ emission mainly originates in the polycyclic aromatic hydrocarbons (PAHs), which are destroyed inside an H II region, it reveals the presence of a photodissociation region (PDR; Hollenbach & Tielens 1997). The emission at $24 \mu\text{m}$ shows the dust heated by the energetic stellar photons while $250 \mu\text{m}$ data trace the cold dust big grains (BG) emission.

A remarkably strong source is readily observed at $(l, b) = (25^\circ 8, 0^\circ 24)$ in Fig. 5. This source, listed as G025.7961+00.2403 in the MSX catalog, is classified as a compact H II region based on its infrared colors. We will discuss its nature and possible origin in Section 4.2.

3.3.1 Dust temperature maps

Dust temperatures in the region were estimated using the emission at 70 and $160 \mu\text{m}$. In a far infrared (FIR) image, the dust temperature (T_d) in each pixel can be obtained assuming that the dust in a single beam is isothermal and that the observed ratio of 70 to $160 \mu\text{m}$ is due to blackbody radiation from dust grains at T_d modified by a power law emissivity. The method used to calculate the dust color temperature is the one used by Schnee et al. (2005). The $70 \mu\text{m}$ image was convolved to the resolution of the $160 \mu\text{m}$ image.

The flux density emission at a wavelength λ_i is given by

$$F_i = \frac{2hc}{\lambda_i^3 (e^{hc/(\lambda_i k T_d)} - 1)} N_d \alpha \lambda_i^{-\beta} \Omega_i \quad (1)$$

where N_d represents the column density of dust grains, α is a constant that relates the flux to the dust optical depth, β is the emissivity spectral index, and Ω_i is the solid angle subtended at λ_i by the detector.

Assuming that the dust emission is optically thin at 70 and $160 \mu\text{m}$ and that $\Omega_{70} \sim \Omega_{160}$, and adopting an index of $\beta = 2$ we can write the ratio, R , of the flux densities as

$$R = (0.4)^{-(\beta+3)} \frac{e^{90/T_d} - 1}{e^{205/T_d} - 1} \quad (2)$$

The dust temperature, T_d , is derived from this equation. Fig. 6 shows the spatial distribution of the dust color temperature, which varies from 20 K to 31 K. The uncertainties were estimated to be about $\sim 10 - 15\%$. The map shows a clear temperature gradient from the central regions (the inner arc-shaped structure, where the ionizing stars are located) to the periphery of the complex, while low temperatures (~ 23 K) are measured at the location of the molecular clumps (see Section 3.4).

3.4 Millimeter and sub-millimeter emission

3.4.1 Carbon monoxide emission

In Fig. 7 (panel *a*) we show the $^{13}\text{CO}(1-0)$ emission distribution map integrated within the velocity interval from 106.6 km s^{-1} to 116.6 km s^{-1} . The molecular gas at this velocity interval depicts a partially arc-shaped structure, with the strongest emission coincident with the IR emission (see Sect. 3.3). This velocity interval is coincident with the velocity of the RRLs detected in the region (see Sect. 2). In panel *b*, we show a composite image of the $8 \mu\text{m}$ emission with the $^{13}\text{CO}(1-0)$ emission. The molecular gas shows an excellent morphological correspondence with the infrared emission,

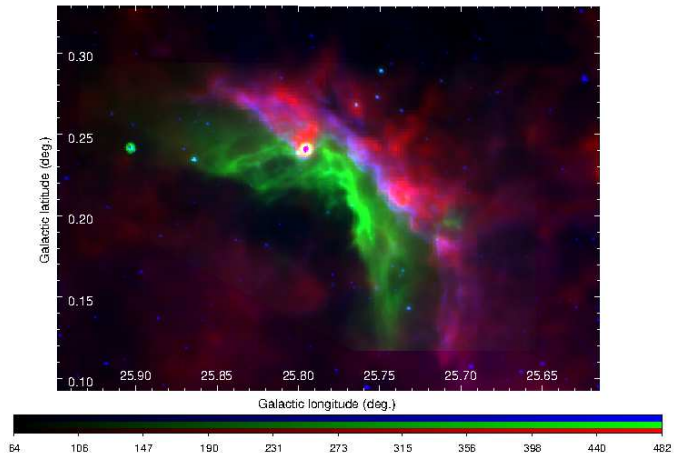


Figure 5. RGB image of G25.8700+0.1350 and surroundings. Red: emission at $250 \mu\text{m}$ (Herschel); green: emission at $24 \mu\text{m}$ (Spitzer); and blue: emission at $8 \mu\text{m}$ (Spitzer).

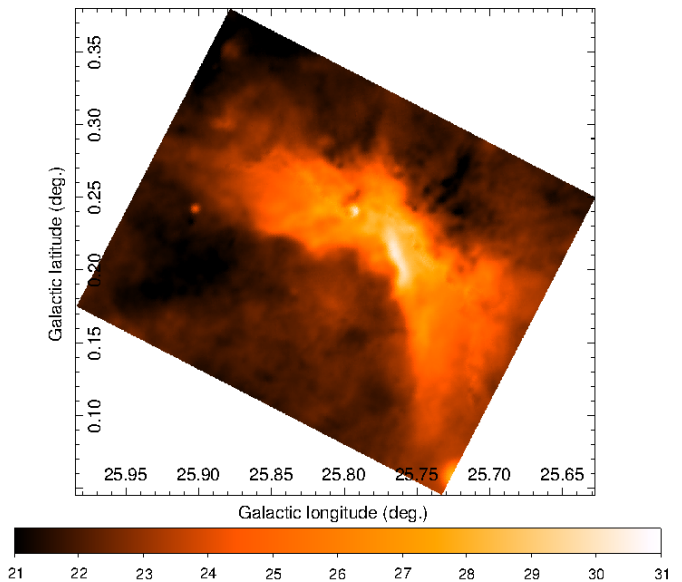


Figure 6. Color temperature map based on emission at 70 and $160 \mu\text{m}$. Color bar units are expressed in K.

which indicates that the molecular component is being ionized by a stellar source (or sources) at lower Galactic Longitude giving rise to a PDR. The presence of strong HI emission almost between the radio continuum and the molecular emission (see Figs. 4 and 1) suggests the existence of a central neutral gas layer between the ionized gas and the molecular gas giving additional support to the PDR scenario. The molecular emission shows a sharp arc-shaped cutoff in the direction of the radio continuum emission while the intensity of the emission decreases smoothly toward the center of the molecular cloud. This layout, which is indicative of a density gradient in the molecular distribution, suggests that the molecular gas has undergone ionization and has probably been compressed on the front side as a result of the expansion of the ionization front and/or by the action of winds of the powering star/s. The incomplete shell structure of the molecular component and the location of the brightest

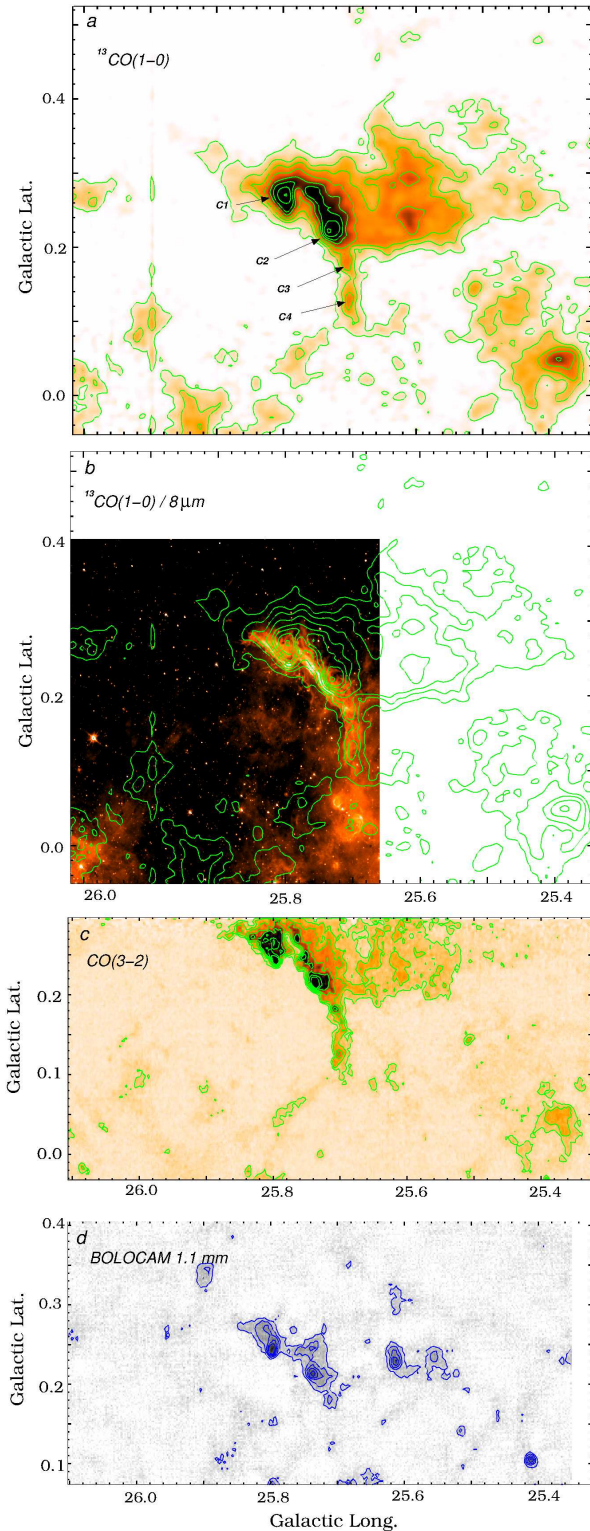


Figure 7. *Panel a:* $^{13}\text{CO}(1-0)$ emission map in the velocity range from 106.6 km s^{-1} to 116.6 km s^{-1} . Contour levels start from 0.2 K km s^{-1} with a contour spacing of 0.2 K km s^{-1} . The positions of molecular clumps C1 and C2 are indicated (see text). *Panel b:* Composite image showing the emission of the $^{13}\text{CO}(1-0)$ line (green contours) over the *Spitzer* $8 \mu\text{m}$ emission (red colour). *Panel c:* $\text{CO}(3-2)$ emission map in the velocity range from 106.6 km s^{-1} to 116.6 km s^{-1} . Contour levels start from 1 K km s^{-1} with a contour spacing of 1 K km s^{-1} . *Panel d:* Bolocam 1.1 mm emission. Contour levels start from $100 \text{ mJy beam}^{-1}$ ($\sim 3\sigma$) with a contour spacing of $100 \text{ mJy beam}^{-1}$.

molecular emission (behind the radio continuum emission at 1420 MHz) give further support to the previously proposed scenario of an H II region density bounded toward higher Galactic longitudes and ionization bounded toward lower Galactic longitudes. In the panel *c* of Fig. 7 we show the $\text{CO}(3-2)$ emission distribution in the region, which shows a similar feature.

It is clear from Fig. 7 that the molecular emission is not uniformly distributed, and several clumps can be distinguished in the brightest region, next to the ionization front. From the present data, it is difficult to ascertain whether these clumps are preexisting concentrations in the molecular structure, or instead they were formed by the accumulation of molecular gas due to the expansion of the ionization front and/or the action of stellar winds. Observational evidence (see previous paragraph) suggests the latter scenario, although for the case of C1, its cometary shape in the continuum emission at 1.1 mm (see Sect. 3.4.2) might indicate that this clump was previously formed.

The physical properties of these clumps must be estimated if a study of the molecular gas is intended. In the following analysis we will concentrate only on the molecular clumps located along the PDR, which are those very likely formed by the expansion of the ionized gas over the parental molecular cloud. These clumps will be hereafter dubbed as clumps C1, C2, C3, and C4. It is worth to point out that clumps C1 and C2 were identified by Anderson & Bania (2009) as the molecular components of $\text{U25.80}+0.24$ and $\text{C25.77}+0.21$, respectively. The location and size of clump C1 is coincident with the MSX source $\text{G025.7961}+00.2403$ and the bright IR source reported at $8, 24,$ and $250 \mu\text{m}$ in Sect. 3.3 (see Fig. 5).

In Table 2 we present some physical properties derived for the CO clumps. We define the area of each clump (A_{clump} , Col. 3) by the contour level corresponding to half the ^{13}CO peak emission (T_{peak}^{13} , Col. 5). The optical depth of the ^{13}CO emission (τ^{13} , Col. 5) and the ^{13}CO column density ($N(^{13}\text{CO})$) were calculated from

$$\tau^{13} = -\ln \left(1 - \frac{T_{\text{peak}}^{13}}{5.29 J[T_{\text{exc}}] - 0.164} \right) \quad (3)$$

and

$$N(^{13}\text{CO}) = 2.42 \times 10^{14} \tau^{13} \frac{\Delta v T_{\text{exc}}}{1 - e^{(-5.29/T_{\text{exc}})}} \text{ (cm}^{-2}\text{)} \quad (4)$$

where $J[T(\text{K})] = 1/(e^{5.29/T(\text{K})} - 1)$, Δv is the FWHM line width, and T_{exc} is the excitation temperature of the $\text{J}=1 \rightarrow 0$ transition of the ^{13}CO (Col. 6). The excitation temperature is usually estimated by the peak temperature of the optically thick $\text{CO}(1-0)$ emission, through the equation

$$T_{\text{exc}} = \frac{5.53}{\ln [1 + 5.53/(T_{\text{peak}}(\text{CO}) + 0.819)]} \text{ (K)} \quad (5)$$

Since no $\text{CO}(1-0)$ line data with spatial resolution better than $\sim 9'$ is available for this quadrant of the Galaxy (Dame, Hartmann & Thaddeus 2001), we made use of the empirical relation

$$T_{\text{peak}}(\text{CO}(1-0)) = \frac{T_{\text{peak}}(\text{CO}(3-2)) + 0.222}{0.816} \quad (6)$$

derived by Oka et al. (2012) for the Galactic center. Then, the H_2 column density ($N(\text{H}_2)$, Col. 8) was derived using $N(\text{H}_2) / N(^{13}\text{CO}) = 5 \times 10^5$ (Dickman 1978). The peak optical depth (τ_{peak}^{13}) and peak column density ($N(\text{H}_2)_{\text{peak}}$) are indicated in Cols. 9 and 10, respectively.

The molecular mass was calculated using

$$M(\text{H}_2) = (m_{\text{sun}})^{-1} \mu m_{\text{H}} \sum A_{\text{clump}} N(\text{H}_2) d^2 \text{ (M}_{\odot}\text{)} \quad (7)$$

Table 2. Physical properties derived for the CO clumps.

	A_{clump} (10^{-6} ster)	R_{eff} (10^{19} cm)	V_{LSR} (km s^{-1})	T_{peak}^{13} (K)	T_{exc} (K)	τ^{13}	$N(\text{H}_2)$ (10^{22} cm^{-2})	τ_{peak}^{13}	$N(\text{H}_2)_{\text{peak}}$ (10^{22} cm^{-2})	M_{H_2} ($10^4 M_{\odot}$)	n_{H_2} (10^3 cm^{-3})	$N_{\text{int}}(\text{H}_2)$ (10^{22} cm^{-2})	M_{int} ($10^4 M_{\odot}$)
C1	0.98	1.12	110.3	7.9	46.5	0.06	3.2	0.19	9.9	2.8	2.1	2.6	0.8
C2	2.05	1.62	110.6	8.1	32.1	0.08	2.0	0.31	7.9	3.6	0.9	2.3	1.1
C3	0.23	0.54	111.6	4.8	24.8	0.05	0.8	0.24	3.7	0.16	1.1	1.1	0.3
C4	0.83	1.03	111.7	4.4	16.5	0.12	0.9	0.42	3.1	0.31	0.3	0.9	0.3

where m_{sun} is the solar mass ($\sim 2 \times 10^{33}$ g), μ is the mean molecular weight, which is assumed to be equal to 2.8 to allow for a relative helium abundance of 25%, m_{H} is the hydrogen atom mass ($\sim 1.67 \times 10^{-24}$ g), and d is the distance (estimated to be 6.5 kpc; Section 3.1). The volume density (n_{H_2} , Col. 12) was estimated considering a spherical geometry, as

$$n_{\text{H}_2} = \frac{M_{\text{H}_2}}{4/3 \pi R_{\text{eff}}^3 \mu m_{\text{H}}} \quad (8)$$

where R_{eff} (Col. 2) is the effective radius of the clump, estimated as $R_{\text{eff}} = \sqrt{A_{\text{clump}}/\pi}$

A different approach to estimate the column density can be made using the CO(3-2) integrated intensity emission.

$$N_{\text{int}}(\text{H}_2) = X \times \int \frac{T(\text{CO}(3-2)) dv}{0.7}, \quad (9)$$

where X is an empirical factor that has been shown to be roughly constant for Galactic molecular clouds. For the the $^{12}\text{CO}(1-0)$ line, the X value is about 1.9×10^{20} K km s^{-1} (Strong & Mattox 1996). Since we use the integrated intensity emission of the CO(3-2) line, we need to adjust the value of $N_{\text{int}}(\text{H}_2)$ using a correcting factor of ~ 0.7 (Oka et al. 2012). Hence, the integrated mass (M_{int}) is calculated using Eqs. 7 and 9.

3.4.2 Continuum 1.1 mm emission

The continuum emission at 1.1 mm is usually dominated by optically thin thermal emission from cold dust embedded in dense material (e.g. dense star-forming cores/clumps and filaments), turning this emission into one of the most reliable tracers of dense molecular gas.

In the panel *d* of Fig. 7 we show the 1.1 continuum emission image obtained from the Bolocam survey. As expected, the emission appears concentrated towards the position of the PDR. Three bright structures can be discerned coincident with the CO clumps C1, C2, and C3. For the sake of clarity, we will also refer to these structures as C1, C2, and C3. C1 and C2 were identified as G025.797+00.245 and G025.737+00.213, respectively in the catalog of Bolocam Galactic Plane Survey (BGPS) sources (Shirley et al. 2013). The presence and location of these submillimeter sources along the border of the H II region is another confirmation for the existence of high-density molecular gas, which was probably accumulated due to the expansion of the ionization front over the molecular environment. This makes clumps C1, C2, and C3 excellent candidates to search for star formation activity; a special mention deserves C1, whose cometary shape suggests the existence of a pre-existing molecular clump where an ionized boundary layer (IBL) originated by nearby O-type stars may be acting to induce the gravitational collapse. Triggered star formation scenarios will be further tested on the regions of C1, C2, and C3 (see Sect. 4.2.2).

Table 3. Parameters derived from the Bolocam 1.1 mm emission.

	T_{dust} (K)	$M_{\text{(tot)}}$ ($10^4 M_{\odot}$)	N_{H_2} (10^{22} cm^{-2})
C1	25.4	2.8	3.5
C2	24.0	3.4	2.6
C3	25.6	0.02	1.1

We estimated the total ($\text{H}_2 + \text{dust}$) mass of C1, C2, and C3 from their integrated 1.1 mm emission, assuming that the emission is optically thin, and using the equation of Hildebrand (1983),

$$M_{\text{(tot)}} = R \frac{S_{1.1\text{mm}} d^2}{\kappa_{1.1\text{mm}} B_{1.1\text{mm}}(T_{\text{dust}})} \quad (10)$$

where R is the gas-to-dust ratio, assumed to be 186 (Draine et al. 2007), $S_{1.1\text{mm}}$ is the flux density, d is the distance (6.5 kpc), $\kappa_{1.1\text{mm}}$ is the dust opacity per unit mass at 1.1 mm assumed to be $1.0 \text{ cm}^2 \text{ g}^{-1}$ (estimated for dust grains with thin ice mantles in cold clumps; Ossenkopf & Henning 1994), and $B_{1.1\text{mm}}(T_{\text{dust}})$ is the Planck function for a temperature T_{dust} . The beam-averaged column density (N_{H_2}) of sources C1, C2, and C3 were calculated using

$$N_{\text{H}_2} = R \frac{I_{\text{peak}}}{\Omega_{\text{beam}} \kappa_{1.1\text{mm}} \mu m_{\text{H}} B_{1.1\text{mm}}(T_{\text{dust}})}. \quad (11)$$

where I_{peak} is the 1.1 mm continuum emission peak intensity, Ω_{beam} is the beam solid angle ($\pi \theta_{\text{HPBW}}^2 / 4 \ln(2)$), μ is the mean molecular weight (assumed to be 2.8 considering a relative helium abundance of 25%), and m_{H} is the mass of the hydrogen atom.

The estimated masses, column densities, and dust temperature used for the calculations (obtained from Fig. 6), are listed in Table 3. A direct comparison between Tables 2 and 3 shows a good agreement in masses and densities for C1 and C2. A discrepancy, nonetheless, is observed in the estimated masses for C3, very likely due to uncertainties in the estimation of the clump's boundaries.

4 DISCUSSION

4.1 Origin of the structure

In this Subsection we attempt to find the stars responsible of the origin of G25.8700+0.1350. Considering that early-type high-mass stars have a major importance in perturbing the interstellar medium, we performed a search for such stars in the whole area by inspecting every catalog available, but we obtained negative results. The paucity of candidate stars can be explained by the high absorption produced by the gas and dust column intervening up to the distance of 6.5 kpc, which can turn even bright early-type stars hard to detect. Taking into account that the extinction in the visual band is on the order of 1.8 magnitudes per kiloparsec near the Galactic plane

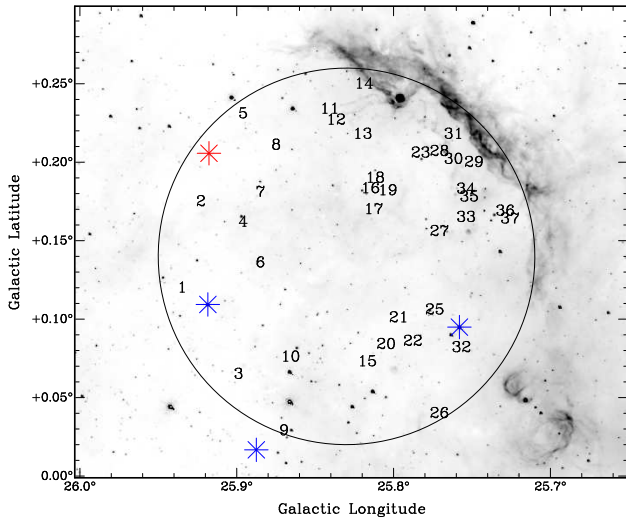


Figure 8. Spitzer emission at $8\ \mu\text{m}$. The circle shows the region considered in the search for the exciting stars. The red asterisk indicates the location of the WR star HDM40, while the numbers correspond to the ID number of the 2MASS sources given in the first column of Table 5. The blue asterisks show the location of the three RSGs present in the region.

(Whittet 2003), the visual absorption for a distance of 6.5 ± 1.0 kpc would be between 10 and 13.5 mag.

Another estimation for the visual absorption A_V can be inferred using the Galactic extinction model developed by Chen et al. (1999). For positive Galactic latitudes, they propose the relation

$$\frac{E(B - V)(D, l, b)}{E(B - V)(\infty, l, b)} = 1 - \exp\left(-\frac{D \sin b}{h}\right)$$

where $E(B - V)(\infty, l, b)$ is the total reddening in the line of sight ($D = \infty$), and h is the scale height of the Galactic Plane absorbing dust, $h = 117.7 \pm 4.7$ pc (Kos et al. 2014). To apply this procedure we first inspected the infrared emission distribution in the region of G25.8700+0.1350 to pick up the region where the exciting stars are more probably located. The H II region has an arc-like shape, hence the exciting stars are expected to appear near its curvature center. In Fig. 8 the region used to look for the ionizing stars is indicated. The value of $E(V - B)(\infty, l, b)$ was obtained using the dust map of the Galaxy constructed by Schlafly & Finkbeiner (2011). Assuming $A_V = 3.1 E(B - V)$, we estimated that the visual absorption in the region is in the range between 10 and 16 mag. This high extinction can explain why the ionized region, being very bright in the radio continuum, is not visible at optical wavelengths, and implies that any candidate early-type ionizing star/s must be searched for in infrared wavelengths.

Several Wolf-Rayet (WR) stars have been recently identified in the infrared by Mauerhan, Van Dyk & Morris (2011). Among them, there is one located at $(l, b) = (25^\circ 92', 0^\circ 21')$ (red asterisk in Fig. 8), which could be related to G25.8700+0.1350. This object is the 2MASS source 18375149-0608417 and was identified as HDM40 and classified as a WC9d star, since strong evidence has been found of thermal dust emission associated. Mauerhan, Van Dyk & Morris (2011) estimated for HDM40 a photometric distance of 4.9 kpc, with an uncertainty probably up to 25% – 40%. The authors claim, however, that this distance should be taken with caution, since the probable thermal dust emission from this star can make the adopted colors and K_s -band absolute photometry not reliable.

Red supergiants can be used to trace recent high-mass star formation even in heavily obscured regions. These high-mass stars are young (between 8 and 25 Ma; Ekström et al. 2013) and very luminous (from $10^{4.5}$ to $10^{5.8} L_\odot$). However, unlike ionizing high-mass stars, RSGs present late spectral types (K and, mostly, M) and red colours. Therefore, they are significantly brighter in infrared bands, and they are more accessible targets for spectroscopic surveys in such bands. In consequence, RSGs are a powerful tool to study highly-extinguished high-mass populations. There are two large high-mass clusters close to G25.8700+0.1350: RSGC1 ($l = 25^\circ 27'$, $b = -0^\circ 16'$; Figer et al. 2006; Davies et al. 2008) and RSGC2 ($l = 26^\circ 19'$, $b = -0^\circ 07'$; Davies et al. 2007). Due to their high extinctions (between 11 and 26 mag in V), the only stellar components observable in them are RSGs. These two clusters present radial velocities ($123.0 \pm 1.0 \text{ km s}^{-1}$ and $109.3 \pm 0.7 \text{ km s}^{-1}$, respectively) and thus kinematic distances (6.6 ± 0.9 kpc and $5.8^{+1.9}_{-0.8}$ kpc, respectively) compatible with G25.8700+0.1350. Given their high initial masses ($30 \pm 10 M_\odot$ and $40 \pm 10 M_\odot$), estimated through population synthesis models from their current RSG population, they should have hosted a significant number of O stars. However, given that the clusters have ages of 12 ± 2 Ma and 17 ± 3 Ma, largely exceeding typical lifetimes of O-type stars, these latter are not expected to exist currently in the clusters. Thus, these clusters are necessarily older than G25.8700+0.1350, where a significant number of O stars is required to explain its radio continuum emission.

Despite the difference in age between the clusters and G25.8700+0.1350, it is not unlikely that G25.8700+0.1350 may be related somehow to these clusters. It has been determined that these clusters are part of an extended stellar association (Negueruela et al. 2012), as there is an over-density of RSGs around them having compatible radial velocities, which is indicative of intense high-mass star forming activity in the region. In fact, the center of G25.8700+0.1350 is located between RSGC1 and RSGC2 (see Figure 9), separated of them by $39' 8''$ and $22' 6''$, respectively. At the estimated distance of G25.8700+0.1350, 6.5 ± 1 kpc, these separations correspond to a *minimum* physical distances of 75^{+12}_{-11} and 43^{+6}_{-7} pc. Moreover, G25.8700+0.1350 has a radius of about $8' 5''$ (16 pc). Therefore, the edges of G25.8700+0.1350 are even closer to these clusters. Considering that both clusters are separated by $54' 6''$ (103 pc at the distance of G25.8700+0.1350) and since they seem to belong to the same association, it is unlikely that a high-mass star forming region as G25.8700+0.1350 were not related to them and to the over-density of RSGCs around them. Moreover, the age difference between the clusters (5 Ma) is not much shorter than the difference that we should expect between RSGC1 and the O-stars in G25.8700+0.1350 (8 – 9 Ma). Therefore, we suggest that G25.8700+0.1350 may represent the youngest star-forming burst of this high-mass star association.

According to evolutionary models (Ekström et al. 2013), only those RSGs of higher masses and luminosities come from the evolution of O stars. Thus, the presence of RSGs related to G25.8700+0.1350 may provide hints about its past O-star population history. Given the over-density of RSGs in this region, we searched for those lying close to G25.8700+0.1350 in the spectroscopic catalogue of Dorda et al. (in preparation). This catalogue provides spectral classifications as well as radial velocities for the stars observed (Dorda et al. 2016). We found three RSGs in the area of G25.8700+0.1350 with compatible radial velocities (see Table 4 and Fig. 8). We used their spectral types together with the work of Levesque et al. (2005) to estimate their $(J - K_s)_0$. Then we calculated $E(J - K_s)$ using the 2MASS photometry and we dereddened K_s applying the calibration of Rieke & Lebofsky

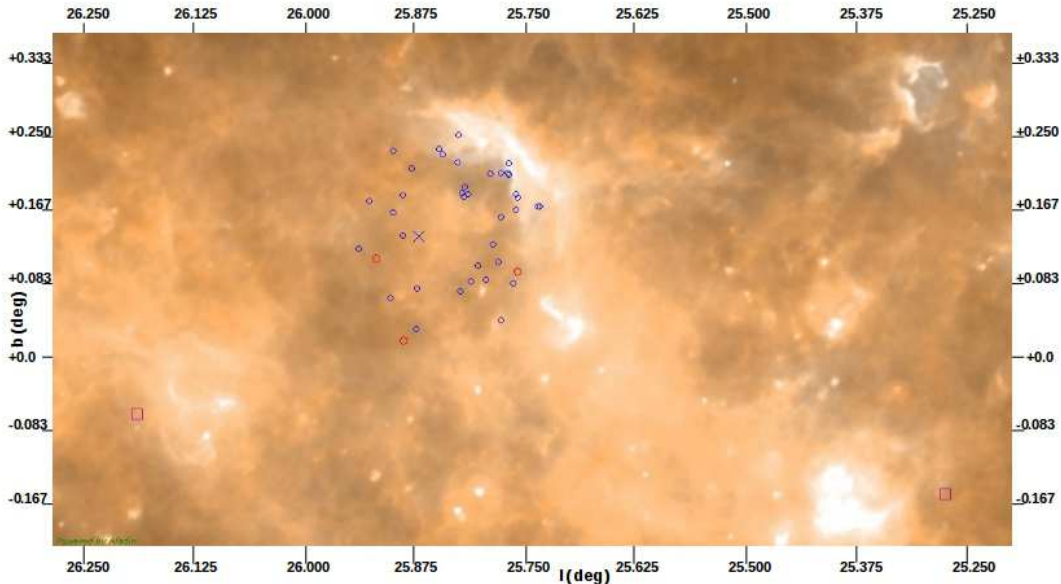


Figure 9. Two colour composite image of G25.8700+0.1350 and surroundings. Blue: PACS 70 μm , Red: PACS 160 μm . The OV source candidates and the RSG known in the region are represented by blue and red circles, respectively. The blue cross indicates the location of the center of G25.8700+0.1350, and the squares the position of the RSG clusters, RSG1 and RSG2.

(1985). We also calculated the bolometric magnitude, using the bolometric corrections proposed by Levesque et al. (2005). Finally, considering that we want to evaluate if these RSGs can be related to G25.8700+0.1350, we used the distance to this H II region to calculate their absolute magnitudes. The masses and corresponding age interval of the RSGs was roughly estimated through M_{bol} , since evolutionary models predict that the luminosity of a RSG depends strongly on its initial mass. For this estimation we used the evolutionary tracks of Geneva (Ekström et al. 2012). Under the distance assumed, the RSGs #2 and #3 are too faint to have evolved from O stars, and thus, they are too old to be related in any way with G25.8700+0.1350. However, for the RSG #1, with a $M_{\text{bol}} \sim -8$, we estimate a $M_i \sim 20 M_{\odot}$ which may well imply a late O star origin (O8V–O9V). A RSG having such mass should have an age between 8 and 9 Ma, which implies that all but the latest O stars have already died if coeval, and thus it should be related to a population whose most massive members at present are O9V stars. In consequence, to confirm the relation between the RSG #1 and G25.8700+0.1350 it would be necessary to know the spectral types and radial velocities of the early-type high-mass stars in this region.

Bearing in mind that early-type high-mass stars have a huge impact onto their surrounding gas via their high rate of energetic photons and stellar winds, the presence of cavities, shells, and H II regions can be used as good tracers for their existence. Thus, as mentioned above, taking into account the morphology of G25.8700+0.1350, we constrained the region where the exciting stars are most probably located (see Fig. 8) and looked for the exciting star candidates using the 2MASS source catalog (Cutri et al. 2003). We selected the candidates using the infrared reddening-free pseudo color $Q_{IR} = (J - H) - 1.83(H - K_s)$, picking those 2MASS sources with $-0.15 < Q_{IR} < 0.1$, indicative of main-sequence stars (Comerón et al. 2002).

We found 1764 sources located inside the region having the best photo-metric quality (ph-qual = AAA) in the three bands J (1.235 μm), H (1.662 μm), and K_s (2.159 μm). Among them, 262

are classified as main-sequence star candidates. Figure 10 shows a color-color diagram depicting the distribution of all sources, with the main-sequence ones plotted in blue. The figure also shows the positions of the dereddened main sequence and giant stars. We located the O-stars into the main sequence using the values given by Martins & Plez (2006), and those given by Tokunaga (2000) and Drilling & Landolt (2000) for late-type stars (B to M). The reddening vector for an early type (O9 V) star is represented by a dashed green line using extinction values from Rieke & Lebofsky (1985). From Fig. 10 we selected the main-sequence candidates lying along the reddening vector between $A_V = 10$ and 16 magnitudes and computed their M_J , M_H , and M_K absolute magnitudes, assuming a distance of $D = 6.5 \pm 1.0$ kpc. We then analyzed whether the estimated magnitudes are in agreement with the absolute magnitudes of O-type stars as given by Martins & Plez (2006). From this comparison we finally found that 37 out of the 1764 2MASS sources could be O-type stars related to G25.8700+0.1350. They are listed in Table 5, indicated by red triangles in Fig. 10 and by white numbers in Fig. 8.

An inspection of their estimated absolute magnitudes (see Columns 8, 9, and 10 of Table 5) shows that several of them could be brighter than an O9V-type star, for which $M_J = -3.48$, $M_H = -3.38$, and $M_K = -3.28$ magnitudes (Martins & Plez 2006), thus suggesting that more than one episode of massive stellar formation has taken place along the last million years.

It is important to note that these 37 sources are just candidates of being responsible of the ionized region, and to confirm this association it is necessary to analyze their spectra. Besides, given the several assumptions involved in the method used to select the O-type star candidates, a certain degree of contamination is to be expected. To estimate the possible contamination level, we applied the same method in a nearby region, covering the same area but centered at (l, b) (26:0, 0:295). We found that 19 out of 1464 2MASS sources (with AAA quality) are OV star candidates (at a distance of 6.5 kpc and with A_V between 10 and 16 mag), which is about half

Table 4. Red supergiants from Dorda et al. (2016) in the area of G25.8700+0.1350 and with compatible radial velocities.

#	2MASS source	l (deg.)	b (deg.)	$V_{\text{LSR}} \pm 1$ (km s $^{-1}$) ^a	Spectral type ^a	K (mag) ^b	M_{bol} (mag) ^b
1	18375756-0620155	025.75802	+00.09493	97	M2.5	-10.77	-7.94
2	18382868-0615304	025.88752	+00.01671	103	M3.5	-8.15	-5.27
3	18381223-0611186	025.91842	+00.10935	101	M2	-10.26	-7.46

^a Spectral type and V_{LSR} are averaged values from the multiple epochs available.

^b The absolute magnitudes were calculated assuming the distance of G25.8700+0.1350 : 6.5 kpc.

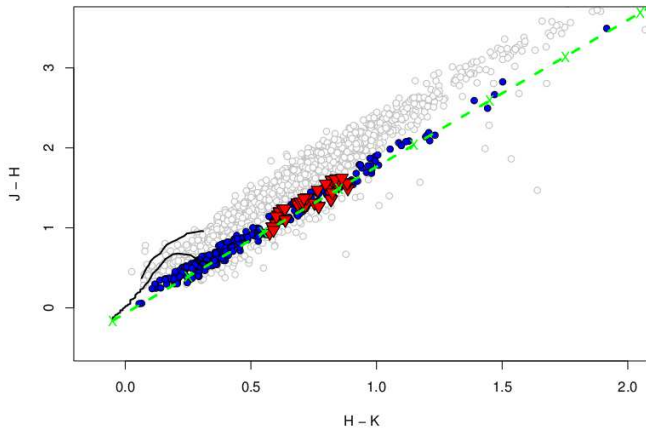


Figure 10. Color-color diagram of the 2MASS sources projected onto the region shown in Fig. 8. Main-sequence candidates are plotted with blue circles. The positions of the dereddened early-type main sequence and giant stars are shown by black lines. The reddening vector for O9 V stars (dashed green line) is indicated. The OV source candidates to be related to G25.8700+0.1350 are represented by red triangles.

the number we found in the G25.8700+0.1350 region, suggesting that the unrelated objects are probably less than 19.

As mentioned in Section 3.2.1, the number of ionizing photons needed to keep the region ionized is very high, $N_{\text{UV}} = (5.0 \pm 1.6) \times 10^{49} \text{ s}^{-1}$. Such amount of UV photons could be supplied by several early-type stars, like 3 O5V, 12 O7V, or 63 O9V stars (Martins, Schaerer & Hillier 2005). Moreover, since in the estimation of N_{UV} the effect of the dust is not taken into account, these figures are just lower limits. In this context, we conclude that most of the 37 2MASS sources found as O-type star candidates could be indeed related to G25.8700+0.1350. Finally, the presence of at least one supergiant suggests that there have been several SN in the area. The absence of catalogued SNRs within this region could be explained either if the explosions occurred $\geq 10^5$ years ago and the remnants have dissipated into the ISM, or the putative SNRs are confused with line-of-sight emission from other sources along this complicated direction of the Galaxy, towards the Galactic Plane. However, although no detected directly, shock waves driven by past SN explosions must have contributed to shape the ISM and could explain the asymmetry of the shell displayed by G25.8700+0.1350.

4.2 Star formation activity in the region

In what follows, we will study if recent star formation activity has taken place in the vicinity of G25.8700+0.1350 to disen-

gle whether seeming expanding motions of the H II region could have triggered star formation. For this purpose, we will try to detect all Young Stellar Object candidates (cYSOs) around the region and analyze their position with respect to the ionized gas and to the molecular condensations.

4.2.1 Identification of Young Stellar Object candidates

Primary tracers of stellar formation activity were searched for using the MSX Infrared Point Source Catalogue (Egan, Price & Kraemer 2003), the WISE All-Sky Source Catalogue (Wright et al. 2010), and the GLIMPSE point source catalog (Benjamin et al. 2003). MSX sources were selected if their variability and reliability flags were zero and the flux quality Q was above 1 in all four bands. WISE sources with photometric flux uncertainties above 0.2 mag and signal-to-noise ratio lower than 7 in the W1, W2, and W3 bands, were rejected. Finally, Spitzer sources were kept if their photometric uncertainties were lower than 0.2 mag in all four IRAC bands.

Within a 9-arcmin radius circle centered at $(l, b) = (25^{\circ}83, 0^{\circ}18)$, a total of 3 MSX, 511 WISE, and 1716 Spitzer sources have been found fulfilling the selection criteria above. To identify the cYSOs among these sources, we adopted the classification scheme described in Lumsden et al. (2002), Koenig et al. (2012), and Gutermuth et al. (2009) for the MSX, WISE, and IRAC data, respectively. Several sources were found to qualify for cYSOs, and are listed in Table 6. The infrared colors of MSX sources permit to discern between high-mass young stellar object (MYSO) candidates and compact H II region (CHII) candidates (Lumsden et al. 2002). Two of the MSX sources selected in this region belong to this latter class.

Before attempting to identify the cYSOs from the listed WISE and Spitzer sources, we selected the non-YSO sources with excess infrared emission, such as PAH-emitting galaxies, broad-line active galactic nuclei (AGNs), unresolved knots of shock emission, and PAH-emission features. A total of 67 and 132 WISE and Spitzer sources, respectively, were dropped from the lists. Among the remaining 444 WISE and 1584 Spitzer sources, 13 (4 WISE and 9 Spitzer) were identified as Class I sources (i.e. sources where the IR emission arises mainly from a dense infalling envelope, including flat spectrum objects) and 63 (56 WISE and 16 Spitzer) as Class II sources (i.e. pre-main-sequence stars with optically thick disks).

In the case of the WISE sources identified as cYSOs, we discarded those not compatible with T Tauri star candidates. For this purpose, we checked if the 56 sources previously classified Class II stars with photometric errors lower than 0.2 in WISE band 4 had blue colors in excess, i.e. if their W1, W3, and W4 magnitudes satisfy that $W1 - W3 \leq -1.7(W3 - W4) + 4.3$ (Koenig et al. 2012). Among the 56 Class II sources found, we have rejected 9 based on this last criterion. On the other hand, protostellar objects with in-

Table 5. Exciting star candidates parameters.

#	2MASS source	l (deg.)	b (deg.)	J (mag)	H (mag)	K_s (mag)	$M_J^{(*)}$ (mag)	$M_H^{(*)}$ (mag)	$M_K^{(*)}$ (mag)
1	18381209-0609575	25.938	0.12	15.087	13.497	12.662	-1.78/ - 3.46	-2.27/ - 3.29	-2.50/ - 3.16
2	18375910-0609061	25.926	0.175	14.589	13.298	12.611	-2.28/ - 3.96	-2.47/ - 3.49	-2.55/ - 3.21
3	18381995-0613242	25.902	0.065	14.72	13.409	12.656	-2.14/ - 3.82	-2.36/ - 3.38	-2.51/ - 3.17
4	18375890-0610528	25.899	0.162	13.817	12.803	12.217	-3.05/ - 4.73	-2.96/ - 3.98	-2.95/ - 3.61
5	18374388-0609002	25.899	0.231	14.328	13.185	12.583	-2.54/ - 4.22	-2.58/ - 3.60	-2.58/ - 3.24
6	18380328-0612113	25.888	0.136	13.141	11.939	11.325	-3.72/ - 5.40	-3.83/ - 4.85	-3.84/ - 4.50
7	18375349-0610555	25.888	0.181	13.54	12.214	11.508	-3.32/ - 5.00	-3.55/ - 4.57	-3.66/ - 4.32
8	18374590-0610389	25.878	0.211	13.664	12.286	11.564	-3.20/ - 4.88	-3.48/ - 4.50	-3.60/ - 4.26
9	18382436-0615561	25.873	0.029	14.888	13.318	12.429	-1.98/ - 3.66	-2.45/ - 3.47	-2.74/ - 3.40
10	18381429-0614414	25.872	0.076	14.964	13.358	12.522	-1.90/ - 3.58	-2.41/ - 3.43	-2.64/ - 3.30
11	18373768-0611408	25.847	0.234	14.287	12.69	11.868	-2.58/ - 4.26	-3.07/ - 4.09	-3.30/ - 3.96
12	18373856-0612053	25.843	0.227	14.89	13.341	12.543	-1.97/ - 3.65	-2.42/ - 3.44	-2.62/ - 3.28
13	18373870-0613133	25.826	0.218	13.759	12.657	12.02	-3.11/ - 4.79	-3.11/ - 4.13	-3.14/ - 3.80
14	18373172-0612247	25.825	0.25	14.141	13.205	12.63	-2.72/ - 4.40	-2.56/ - 3.58	-2.53/ - 3.19
15	18380952-0617237	25.823	0.073	13.026	11.741	11.029	-3.84/ - 5.52	-4.02/ - 5.04	-4.14/ - 4.80
16	18374551-0614256	25.821	0.184	13.46	12.137	11.44	-3.40/ - 5.08	-3.63/ - 4.65	-3.72/ - 4.38
17	18374618-0614401	25.819	0.18	13.48	12.24	11.605	-3.38/ - 5.06	-3.52/ - 4.54	-3.56/ - 4.22
18	18374373-0614273	25.818	0.19	14.679	13.119	12.281	-2.19/ - 3.87	-2.65/ - 3.67	-2.88/ - 3.54
19	18374508-0614503	25.814	0.182	13.949	12.593	11.774	-2.92/ - 4.60	-3.17/ - 4.19	-3.39/ - 4.05
20	18380578-0617446	25.811	0.084	14.849	13.225	12.363	-2.02/ - 3.70	-2.54/ - 3.56	-2.80/ - 3.46
21	18380121-0617407	25.803	0.101	14.098	12.539	11.656	-2.77/ - 4.45	-3.23/ - 4.25	-3.51/ - 4.17
22	18380355-0618358	25.794	0.086	14.121	13.148	12.558	-2.74/ - 4.42	-2.62/ - 3.64	-2.61/ - 3.27
23	18373718-0615341	25.789	0.206	14.584	13.051	12.202	-2.28/ - 3.96	-2.71/ - 3.73	-2.96/ - 3.62
24	18375398-0617554	25.786	0.126	14.725	13.284	12.46	-2.14/ - 3.82	-2.48/ - 3.50	-2.70/ - 3.36
25	18375763-0618478	25.78	0.106	13.171	11.859	11.173	-3.69/ - 5.37	-3.91/ - 4.93	-3.99/ - 4.65
26	18381156-0620453	25.777	0.04	14.281	13.011	12.241	-2.58/ - 4.26	-2.75/ - 3.77	-2.92/ - 3.58
27	18374651-0617334	25.777	0.156	14.933	13.454	12.646	-1.93/ - 3.61	-2.31/ - 3.33	-2.52/ - 3.18
28	18373564-0616112	25.777	0.207	14.042	12.755	12.037	-2.82/ - 4.50	-3.01/ - 4.03	-3.13/ - 3.79
29	18373488-0616374	25.769	0.206	15.011	13.52	12.634	-1.85/ - 3.53	-2.24/ - 3.26	-2.53/ - 3.19
30	18373506-0616423	25.768	0.205	15.061	13.442	12.602	-1.80/ - 3.48	-2.32/ - 3.34	-2.56/ - 3.22
31	18373224-0616205	25.768	0.218	14.87	13.396	12.63	-1.99/ - 3.67	-2.37/ - 3.39	-2.53/ - 3.19
32	18380088-0620213	25.763	0.082	14.748	13.379	12.668	-2.12/ - 3.80	-2.39/ - 3.41	-2.50/ - 3.16
33	18374279-0618120	25.76	0.165	14.225	12.926	12.202	-2.64/ - 4.32	-2.84/ - 3.86	-2.96/ - 3.62
34	18373904-0617427	25.76	0.183	13.459	12.405	11.805	-3.41/ - 5.09	-3.36/ - 4.38	-3.36/ - 4.02
35	18373971-0617559	25.758	0.179	14.253	13.015	12.388	-2.61/ - 4.29	-2.75/ - 3.77	-2.78/ - 3.44
36	18373913-0619269	25.735	0.169	12.574	11.413	10.804	-4.29/ - 5.97	-4.35/ - 5.37	-4.36/ - 5.02
37	18373896-0619328	25.733	0.169	14.959	13.467	12.662	-1.91/ - 3.59	-2.30/ - 3.32	-2.50/ - 3.16

* Absolute magnitudes estimated for $D = 6.5$ kpc and $A_v = 10/16$ mag.

intermediate/high masses can be identified among Class I sources by additionally requiring their band 3 ($12 \mu\text{m}$) magnitude to be less than 5 (Higuchi et al. 2013). All four Class I WISE sources detected seem to be high-mass protostars, since all of them satisfy this criterion.

The cYSOs remaining in the final list are indicated in Fig. 11 and their fluxes/magnitudes are listed in Table 6.

4.2.2 Spatial distribution of cYSOs and possible formation scenarios

Figure 11 shows that more than half of the cYSOs are found located onto the PDR, with enhanced concentration at the locations of the molecular clumps C1, C2, C3 and C4 (see Column 8 of Table 6), while the rest are seen located projected toward the inner part of the H II region where only faint molecular gas emission is detected at the velocity interval between 100 and 115 km s^{-1} , as delineated by the 0.3 K contour in Fig. 11.

On the other hand, we note that in the direction of the cYSOs located onto C1, C2, C3, and C4 most of the CO profiles show one single radial component and that in the cases where two or

more components are detected, their intensities are considerably lower than the component within the velocity interval between $+108$ and $+120 \text{ km s}^{-1}$. On the contrary, in direction to the rest of the cYSOs, several CO components are observed, as indicated in the last column of Table 6, where the radial velocities of the observed components are shown in decreasing order according to their relative intensities. This suggests that several cYSOs are probably related to molecular gas located at a different distance than G25.8700+0.1350, although the possibility that either they have already destroyed all their natal cloud or that they are not protostellar objects cannot be discarded.

The observed spatial distribution of the cYSOs is a good indicator that the action of G25.8700+0.1350 onto its environs is strong and could have triggered the formation of new stars. The estimated column densities (see Table 2 and 3) are all above the threshold found by André et al. (2011), $N_{H_2} \geq 7 \times 10^{21} \text{ cm}^{-2}$, indicating that star formation may well have taken place in all four clumps. Moreover, the mass-size relationship, which establishes that if $m(r) \geq 870 M_\odot (r/\text{pc})^{1.33}$ the cloud may form high-mass stars (Kauffmann & Pillai 2010), is fulfilled in two of them, C1 and C2.

Table 6. IRAS, MSX, WISE and Spitzer sources found to be YSO candidates.

MSX sources							
#	Designation	(<i>l</i> , <i>b</i>)	F ₈ [Jy] (Q ₈)	F ₁₂ [Jy] (Q ₁₂)	F ₁₄ [Jy] (Q ₁₄)	F ₂₁ [Jy] (Q ₂₁)	Notes
1	G025.7961+00.2403	25° 796, 0° 2403	6.8488 (4)	8.4698 (4)	5.897 (4)	25.377 (4)	CHII, C1
2	G025.7597+00.1933	25° 7597, 0° 193	0.1439 (3)	1.304 (3)	1.0198 (2)	5.11 (4)	CHII
WISE sources							
#	Designation	(<i>l</i> , <i>b</i>)	W1 [mag]	W2 [mag]	W3 [mag]	W4 [mag]	Notes
3	J183729.32-061225.2	25° 820, 0° 258	10.696 ± 0.079	9.186 ± 0.035	4.628 ± 0.021	2.730 ± 0.050	Class I, C1
4	J183726.58-061545.7	25° 765, 0° 243	10.435 ± 0.074	9.416 ± 0.061	4.498 ± 0.107	0.537 ± 0.020	Class I, C2
5	J183728.15-061559.8	25° 765, 0° 235	10.330 ± 0.071	9.329 ± 0.060	4.362 ± 0.094	1.123 ± 0.038	Class I, C2
6	J183730.52-061415.2	25° 795, 0° 240	7.550 ± 0.021	6.522 ± 0.019	1.219 ± 0.073	-2.044 ± 0.016	Class I, C1
7	J183720.07-061447.9	25° 767, 0° 274	9.392 ± 0.026	8.739 ± 0.023	7.279 ± 0.039	4.088 ± 0.042	Class II, C2
8	J183732.00-061425.2	25° 795, 0° 233	10.189 ± 0.04	9.83 ± 0.046	5.602 ± 0.045	0.524 ± 0.022	Class II, C1
9	J183730.15-062034.0	25° 701, 0° 193	11.04 ± 0.058	10.692 ± 0.063	6.218 ± 0.065	1.223 ± 0.030	Class II, C3
10	J183726.91-061930.3	25° 710, 0° 213	11.615 ± 0.14	11.058 ± 0.146	6.721 ± 0.053	3.319 ± 0.064	Class II, C2
11	J183731.83-061404.8	25° 800, 0° 236	9.077 ± 0.029	8.52 ± 0.029	4.707 ± 0.028	0.658 ± 0.055	Class II, C1
12	J183721.37-061325.2	25° 790, 0° 280	9.519 ± 0.028	8.92 ± 0.028	7.497 ± 0.075	3.862 ± 0.029	Class II, C1
13	J183731.37-061402.1	25° 800, 0° 238	8.16 ± 0.024	7.600 ± 0.024	3.877 ± 0.086	-0.978 ± 0.030	Class II, C1
14	J183734.68-062018.6	25° 713, 0° 178	9.999 ± 0.035	9.579 ± 0.046	4.707 ± 0.026	2.802 ± 0.036	Class II, C3
15	J183746.69-062218.8	25° 706, 0° 119	9.345 ± 0.029	9.029 ± 0.027	5.453 ± 0.025	3.673 ± 0.061	Class II, C4
16	J183724.91-061434.8	25° 779, 0° 258	10.15 ± 0.055	9.744 ± 0.069	5.28 ± 0.028	1.853 ± 0.023	Class II, C1
17	J183725.21-061526.0	25° 767, 0° 250	9.638 ± 0.034	9.225 ± 0.04	5.229 ± 0.05	1.53 ± 0.027	Class II, C2
18	J183732.37-061324.2	25° 811, 0° 240	10.864 ± 0.057	10.4 ± 0.073	6.883 ± 0.121	1.286 ± 0.069	Class II, C1
19	J183746.38-062153.6	25° 712, 0° 123	8.308 ± 0.023	7.854 ± 0.023	6.091 ± 0.034	4.188 ± 0.072	Class II, C4
20	J183728.71-061606.4	25° 764, 0° 232	10.173 ± 0.078	9.589 ± 0.053	4.77 ± 0.059	0.898 ± 0.028	Class II, C2
21	J183720.95-061508.7	25° 764, 0° 268	9.939 ± 0.031	9.548 ± 0.032	5.264 ± 0.022	1.967 ± 0.023	Class II, C2
22	J183732.07-062116.5	25° 694, 0° 181	10.792 ± 0.05	9.996 ± 0.045	7.387 ± 0.105	3.731 ± 0.054	Class II, C3
23	J183727.95-061159.4	25° 824, 0° 267	9.5 ± 0.05	8.816 ± 0.032	4.605 ± 0.027	4.878 ± 0.199	Class II, C1
24	J183724.91-061449.6	25° 776, 0° 256	10.77 ± 0.066	10.047 ± 0.067	5.189 ± 0.027	2.492 ± 0.058	Class II, C1
25	J183731.33-061828.3	25° 734, 0° 205	10.262 ± 0.037	9.367 ± 0.033	4.484 ± 0.035	1.442 ± 0.043	Class II, C2
26	J183746.75-062236.7	25° 702, 0° 116	10.389 ± 0.038	9.933 ± 0.035	6.596 ± 0.046	4.499 ± 0.108	Class II, C4
27	J183714.88-061522.2	25° 749, 0° 289	5.587 ± 0.123	4.936 ± 0.064	3.359 ± 0.017	2.074 ± 0.018	Class II, C2
28	J183731.91-062020.5	25° 707, 0° 188	10.895 ± 0.065	9.914 ± 0.046	6.644 ± 0.043	2.424 ± 0.053	Class II, C3
29	J183731.09-060932.4	25° 866, 0° 274	10.868 ± 0.049	10.467 ± 0.046	7.521 ± 0.065	6.633 ± null	Class II, C1
30	J183727.40-061714.7	25° 745, 0° 229	10.352 ± 0.067	9.991 ± 0.041	5.598 ± 0.041	1.654 ± 0.030	Class II, C2
31	J183728.07-061716.6	25° 746, 0° 226	10.597 ± 0.062	10.002 ± 0.044	5.443 ± 0.058	1.17 ± 0.023	Class II, C2
32	J183726.23-061207.7	25° 818, 0° 272	10.883 ± 0.109	10.26 ± 0.076	5.504 ± 0.033	2.608 ± 0.046	Class II, C1
33	J183724.66-061443.1	25° 777, 0° 258	11.037 ± 0.076	10.056 ± 0.071	5.243 ± 0.032	1.973 ± 0.035	Class II, C1
34*	J183732.95-062018.7	25° 710, 0° 185	8.882 ± 0.028	8.419 ± 0.025	4.519 ± 0.021	3.456 ± 0.062	Class II, C3
35	J183725.03-061515.4	25° 770, 0° 252	10.402 ± 0.037	9.728 ± 0.042	5.351 ± 0.053	2.036 ± 0.037	Class II, C1
36	J183730.25-062047.2	25° 698, 0° 191	10.752 ± 0.057	10.298 ± 0.049	7.171 ± 0.135	1.568 ± 0.026	Class II, C3
37	J183725.12-061500.3	25° 774, 0° 254	10.32 ± 0.049	9.947 ± 0.065	5.316 ± 0.029	2.108 ± 0.040	Class II, C1
38	J183721.48-061309.7	25° 794, 0° 282	9.442 ± 0.031	8.765 ± 0.027	6.646 ± 0.032	4.136 ± 0.028	Class II, C1
39	J183723.96-061446.6	25° 775, 0° 260	11.475 ± 0.109	10.898 ± 0.141	7.26 ± 0.148	2.967 ± 0.065	Class II, C1
40	J183805.93-060741.8	25° 959, 0° 160	10.944 ± 0.043	10.569 ± 0.051	7.426 ± 0.116	4.443 ± 0.136	Class II, 100 km s ⁻¹
41	J183810.23-061515.0	25° 856, 0° 087	9.714 ± 0.029	9.305 ± 0.031	7.335 ± 0.086	4.762 ± 0.117	Class II, 30 km s ⁻¹
42	J183817.35-061815.5	25° 825, 0° 0374	9.912 ± 0.028	9.525 ± 0.031	7.433 ± 0.117	4.574 ± 0.060	Class II, 100 km s ⁻¹
43	J183747.97-061326.5	25° 840, 0° 182	9.771 ± 0.03	9.276 ± 0.026	7.603 ± 0.134	5.187 ± 0.136	Class II, 100 km s ⁻¹
44	J183812.35-060918.5	25° 948, 0° 124	8.132 ± 0.035	7.391 ± 0.021	6.202 ± 0.029	4.151 ± 0.039	Class II, 100 km s ⁻¹
45	J183751.67-062025.4	25° 744, 0° 115	8.204 ± 0.026	7.78 ± 0.023	6.24 ± 0.023	1.543 ± 0.060	Class II, 30 and 100 km s ⁻¹
46	J183745.91-060510.9	25° 959, 0° 253	8.994 ± 0.027	8.518 ± 0.023	7.088 ± 0.066	4.981 ± 0.274	Class II, 100 km s ⁻¹
47	J183812.05-061227.1	25° 901, 0° 101	10.487 ± 0.04	9.721 ± 0.036	8.163 ± 0.096	6.295 ± 0.207	Class II, 100 km s ⁻¹
48	J183810.70-060807.3	25° 962, 0° 139	10.579 ± 0.043	10.255 ± 0.038	7.502 ± 0.09	5.793 ± 0.116	Class II, 100 km s ⁻¹
49	J183815.45-061755.5	25° 826, 0° 0470	9.639 ± 0.079	8.95 ± 0.07	6.346 ± 0.118	4.01 ± 0.081	Class II, 100 km s ⁻¹
50	J183743.67-060833.7	25° 905, 0° 235	10.657 ± 0.037	9.818 ± 0.037	7.753 ± 0.115	2.578 ± 0.027	Class II, 70 and 100 km s ⁻¹
51	J183759.17-062006.6	25° 763, 0° 090	6.336 ± 0.05	5.796 ± 0.025	3.14 ± 0.016	1.373 ± 0.024	Class II, 30 and 100 km s ⁻¹
52	J183757.75-061054.6	25° 897, 0° 166	6.126 ± 0.108	5.486 ± 0.06	3.962 ± 0.017	2.626 ± 0.028	Class II, 65 and 100 km s ⁻¹
53	J183752.61-061021.2	25° 895, 0° 189	10.814 ± 0.062	10.115 ± 0.045	8.106 ± 0.102	6.485 ± 0.144	Class II, 65 and 100 km s ⁻¹

Table 6. Continued.

#	Designation	(l, b)	Spitzer sources				Notes
			4.5 μm [mag]	5.8 μm [mag]	8.0 μm [mag]	24 μm [mag]	
54	G025.7443+00.1845	25°744, 0°184	12.156 ± 0.08	11.027 ± 0.06	10.16 ± 0.072	9.955 ± 0.146	Class I
55	G025.7967+00.2764	25°796, 0°276	12.3 ± 0.058	11.463 ± 0.098	10.565 ± 0.095	9.796 ± 0.113	Class I, C1
56	G025.7943+00.2827	25°794, 0°282	9.937 ± 0.05	9.146 ± 0.043	8.395 ± 0.039	7.856 ± 0.045	Class I, C1
57	G025.7619+00.1029	25°762, 0°103	12.421 ± 0.058	10.408 ± 0.11	8.896 ± 0.039	8.025 ± 0.046	Class I, 30, 60, and 100 km s ⁻¹
58	G025.8895+00.0917	25°889, 0°091	13.512 ± 0.088	12.063 ± 0.088	11.088 ± 0.108	10.379 ± 0.085	Class I, 100 and 30 km s ⁻¹
59	G025.7978+00.0736	25°797, 0°073	12.572 ± 0.08	11.321 ± 0.087	10.416 ± 0.074	9.886 ± 0.064	Class I, 30 and 60 km s ⁻¹
60	G025.8564+00.0781	25°856, 0°078	12.506 ± 0.096	11.643 ± 0.061	10.878 ± 0.094	10.567 ± 0.085	Class I, 100, 120, 60, and 30 km s ⁻¹
61	G025.8320+00.0735	25°832, 0°073	13.609 ± 0.128	11.896 ± 0.146	10.567 ± 0.07	9.941 ± 0.057	Class I, 30, 40, 100 km s ⁻¹
62	G025.8991+00.1062	25°899, 0°106	12.735 ± 0.079	11.552 ± 0.08	10.507 ± 0.083	9.378 ± 0.042	Class I, 100, 30, 60 km s ⁻¹
63	G025.7545+00.2578	25°754, 0°257	11.246 ± 0.077	10.262 ± 0.059	9.564 ± 0.055	9.021 ± 0.06	Class II, C2
64	G025.7212+00.2476	25°721, 0°247	8.775 ± 0.043	8.335 ± 0.049	7.761 ± 0.033	7.4 ± 0.032	Class II, C2
65	G025.8269+00.1224	25°827, 0°122	8.544 ± 0.05	8.289 ± 0.041	7.76 ± 0.034	7.405 ± 0.029	Class II, 90, 100, 30 km s ⁻¹
66	G025.7900+00.1191	25°790, 0°119	12.4 ± 0.078	11.738 ± 0.074	11.351 ± 0.1	10.333 ± 0.079	Class II, 30 km s ⁻¹
67	G025.7754+00.1288	25°775, 0°128	8.893 ± 0.041	8.602 ± 0.046	8.338 ± 0.039	7.925 ± 0.033	Class II, 30 km s ⁻¹
68	G025.9598+00.1602	25°959, 0°160	10.815 ± 0.041	10.412 ± 0.079	10.134 ± 0.059	9.238 ± 0.059	Class II, 100 km s ⁻¹
69	G025.9303+00.1309	25°930, 0°131	10.868 ± 0.051	10.298 ± 0.058	9.749 ± 0.059	8.926 ± 0.043	Class II, 100, 60 km s ⁻¹
70	G025.7820+00.0632	25°782, 0°063	9.801 ± 0.06	9.15 ± 0.051	8.59 ± 0.039	7.702 ± 0.029	Class II, 30, 110 km s ⁻¹
71	G025.8833+00.2496	25°883, 0°249	10.020 ± 0.045	9.351 ± 0.053	8.719 ± 0.036	7.873 ± 0.048	Class II, 100, 70 km s ⁻¹
72	G025.8383+00.2416	25°838, 0°241	12.622 ± 0.073	12.022 ± 0.097	11.685 ± 0.151	10.532 ± 0.103	Class II, 100, 70 km s ⁻¹
73	G025.8281+00.1596	25°828, 0°159	12.009 ± 0.095	11.106 ± 0.106	10.454 ± 0.079	9.781 ± 0.061	Class II, 100, 30, 60 km s ⁻¹
74	G025.8786+00.1662	25°878, 0°166	11.467 ± 0.069	11.035 ± 0.129	10.685 ± 0.067	10.099 ± 0.054	Class II, 60, 70, 100 km s ⁻¹
75	G025.8865+00.1622	25°886, 0°162	11.923 ± 0.056	11.406 ± 0.071	10.775 ± 0.097	10.2 ± 0.066	Class II, 60, 70, 100 km s ⁻¹
76	G025.8133+00.1824	25°813, 0°182	11.854 ± 0.111	11.269 ± 0.079	10.983 ± 0.073	10.229 ± 0.08	Class II, 100, 60 km s ⁻¹
77	G025.8548+00.1909	25°855, 0°191	12.254 ± 0.104	11.604999 ± 0.116	11.117 ± 0.088	9.737 ± 0.081	Class II, 100, 60 km s ⁻¹
78	G025.8952+00.1889	25°895, 0°189	10.405 ± 0.04	9.823 ± 0.057	9.148 ± 0.044	8.433 ± 0.034	Class II, 100, 60, 70 km s ⁻¹

4.2.2.1 The Radiative driven implosion scenario. An close inspection of Fig. 11 suggests that the radiation-driven implosion (RDI), could be at work in this region, since the molecular clump labeled C1 exhibits a cometary shape (see Sect. 3.4.2).

Radiative pressure from H II regions push away low density gas more efficiently, and hence faster, than high density gas, thus perturbing the structure and dynamics of molecular clouds. As a result, when an H II region finds dense molecular clumps along its expansion, it may give rise to the formation of bright rim clouds. When this happens, an IBL is developed around the clump and a photo-ionization front is driven into it. The subsequent evolution of the cloud is determined by the pressure balance between the internal molecular pressure and the external pressure of the IBL (Lefloch & Lazareff 1994).

Figure 12 shows an enlarged view of the region of the clump C1. The cometary shape of the molecular cloud, shown through its BOLOCAM emission, is evident, as well as its bright infrared border. Given their location with respect to the head of C1, the 2MASS sources #16, 17, 18 and 19 (asterisks in Fig. 12) are candidates of being the O-type stars creating the IBL.

The cometary shape of the structure suggests that the RDI mechanism could be at work in this molecular cloud. Moreover, the presence of several cYSOs projected onto C1 (see Fig. 11) suggests that a star cluster has formed there and one of them has already given rise to the CHII region G025.7961+00.2403. To ascertain whether this is the case, both inner and outer pressures acting onto the clump have to be estimated and compared.

The pressure in the IBL can be evaluated from the electron density in the boundary layer, n_e , as $P_i = 2 n_e m_H c_i^2$, where $m_H = 1.67 \times 10^{-24}$ g, is the mass of the hydrogen atom and c_i is the sound speed in the ionized gas ($c_i \sim 14$ km s⁻¹). A rough estimation of n_e can be obtained using the spherical model of Mezger & Henderson

(1967) with an appropriate filling factor f to account for the fraction of the assumed sphere that actually contains ionized gas,

$$n_e = 533.5 T_4^{0.175} \nu_{\text{GHz}}^{0.05} S_\nu^{0.5} (f^{1/3} \theta)^{-1.5} D_{\text{kpc}}^{-0.5} \text{cm}^{-3},$$

where S_ν is the measured flux density in Jy, θ the angular width in minutes of arc, T_4 the electron temperature in units of 10^4 K, D_{kpc} the distance in kpc, and ν_{GHz} the frequency in GHz.

Based on the MAGPIS 1.42 GHz image, we obtained a flux density $S_{1.42} = 120 \pm 30$ mJy for the emission observed in the border of C1. Then, assuming a distance of 6.5 ± 1.0 kpc, a temperature of 6120 ± 100 K, the C1 angular width, $\theta = 4 \pm 1$ arcmin and $f = 0.03$, we obtain $n_e = 70 \pm 30$ cm⁻³ and $P_i/k = (3.3 \pm 1.4) \times 10^6$ cm⁻³ K.

As mentioned above, this pressure should be compared with the pressure of the molecular cloud, which can be estimated, assuming that the thermal component can be neglected, from the turbulent velocity dispersion, σ^2 , and the molecular density, ρ_m , as $P_m = \sigma^2 \rho_m$, where σ^2 may be written as $\sigma^2 = \Delta v^2 / (8 \ln 2)$, Δv being the observed velocity line width of the molecular cloud gas. Adopting for C1 the ambient density given in Table 2, $n_{\text{H}2} = 2.1 \times 10^3$ cm⁻³, and $\Delta v = 4.8 \pm 0.7$ km s⁻¹, we infer a molecular pressure $P_m/k = (2.8 \pm 1.2) \times 10^{-6}$ cm⁻³ K, assuming a 30% error in the molecular density.

Since the pressures P_i and P_m obtained for C1 are similar, the ionized and molecular gas seem to be in pressure balance and the propagation of a photoionization-induced shock into the molecular gas might have occurred.

5 SUMMARY

We have carried out a multi-wavelength study of the ionized region G25.8700+0.1350 in order to characterize the physical properties

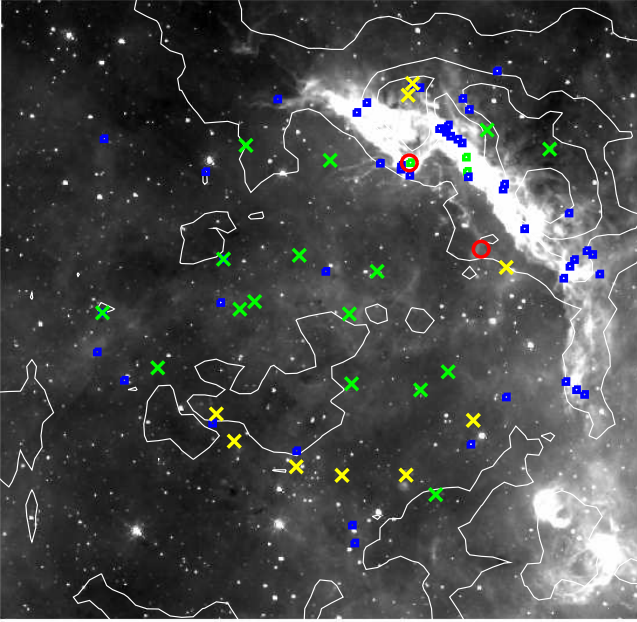


Figure 11. Spitzer $8\ \mu\text{m}$ emission distribution showing the PDR. Contour levels at 0.3, 0.8, 1.0 and 1.3 K delineate the average ^{13}CO emission between 100 and $115\ \text{km s}^{-1}$. The red circles indicate the location of the MSX sources. Green and blue squares correspond to WISE Class I and II cYSO, respectively. Yellow and green crosses indicate Spitzer Class I and II sources, respectively.

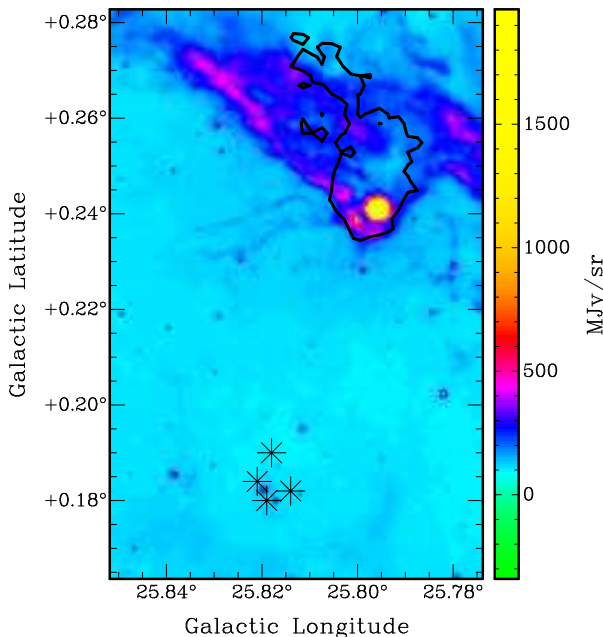


Figure 12. Spitzer image at $8\ \mu\text{m}$ of the region of the C1 source. The contour indicates the 1.1 mm emission at $0.3\ \text{Jy beam}^{-1}$. The four asterisks show the location of the 2MASS sources candidates of being O-type stars (#16, 17, 18, and 19 in Table 5 and Fig. 8).

of the related gas and dust and to investigate its possible origin and role in forming new stars. Based on data obtained from several surveys we arrived to the following results:

(i) Since G25.8700+0.1350 is located in the first Galactic quadrant and close to the tangent point, its distance was not clear. Based on the comparison of H I absorption profiles, in this work we could solve the distance ambiguity and determine a distance of 6.5 ± 1.0 kpc from the Sun, which corresponds to the near distance.

(ii) The region is very bright at 1420 MHz radio continuum. It contains about $2500\ M_{\odot}$ of ionized gas, and at least $5 \times 10^{49}\ \text{ph s}^{-1}$ are needed to keep it ionized. This implies that several O-type stars, which have not been detected yet, should be located in this part of the Galaxy.

(iii) The ^{13}CO (1-0) and 1.1 mm data reveal the presence of four clumps bordering the H II region. These are detected approximately in the velocity range from 106 to $116\ \text{km s}^{-1}$, compatible with the velocity of the RRLs detected in the region. Based on their estimated physical properties, we conclude that all these clumps are capable of forming new stars and, in particular, clumps C1 and C2 may contain high-mass protostars.

(iv) At infrared wavelengths, we identified an unmistakable photo-dissociation region in the interface between the ionized and molecular gas. The Herschel data show that the region is also detected in the far infrared. We found that the dust temperature goes from about 21 K in the cold clumps, up to 31 K in the region more directly exposed to stellar radiation.

(v) Since G25.8700+0.1350 is located in the inner galaxy, where the visual extinction is high, the candidate ionizing stars had to be searched in the infrared. There is one WR star, HDM 40, and one RSG, 18375756-0620155, that may be related to the region. On the other hand, based on color criteria, we identified 37 2MASS sources which could be the O-type ionizing stars.

(vi) Applying different colour criteria, 78 YSO candidates have been identified in the region, of which 44 are projected onto the molecular gas related to G25.8700+0.1350. Based on the observed distribution of both the infrared and molecular emission, we propose that the RDI mechanism has taken place onto C1 and triggered the formation of the high-mass star responsible of the striking CHII region G025.7961+00.2403.

ACKNOWLEDGMENTS

This work is dedicated to the memory of our dear colleague Dr. Gisela Romero. **We are grateful to the referee for his/her very constructive input.** The VGPS is supported by a grant from the Natural Sciences and Engineering Research Council of Canada and from the U.S. National Science Foundation. The National Radio Astronomy Observatory is a facility of the National Science Foundation operated under cooperative agreement by Associated Universities, Inc. This research has made use of the NASA/IPAC Infrared Science Archive, which is operated by the Jet Propulsion Laboratory, California Institute of Technology, under contract with the National Aeronautics and Space Administration. Herschel is an ESA space observatory with science instruments provided by European-led Principal Investigator consortia and with important participation from NASA. This work is partially based on observations made with the Spitzer Space Telescope, which is operated by the Jet Propulsion Laboratory, California Institute of Technology under a contract with NASA. This publication makes use of molecular line data from the Boston University-FCRAO Galactic

Ring Survey (GRS). The GRS is a joint project of Boston University and Five College Radio Astronomy Observatory, funded by the National Science Foundation under grants AST-9800334, AST-0098562, & AST-0100793 This project was partially financed by the Consejo Nacional de Investigaciones Científicas y Técnicas (CONICET) of Argentina under project PIP 01299, PIP 0226, PIP 00356, and PIP 00107, Universidad de La Plata UNLP 2012-2014 PPID/G002 and 11/G120.

References

- Aguirre J. E. et al., 2011, *ApJS*, 192, 4
- Anderson L. D., Bania T. M., 2009, *ApJ*, 690, 706
- Anderson L. D., Bania T. M., Balser D. S., Cunningham V., Wenger T. V., Johnstone B. M., Armentrout W. P., 2014, *ApJS*, 212, 1
- Anderson L. D., Bania T. M., Jackson J. M., Clemens D. P., Heyer M., Simon R., Shah R. Y., Rathborne J. M., 2009, *ApJS*, 181, 255
- André P., Men'shchikov A., Könyves V., Arzoumanian D., 2011, in *IAU Symposium*, Vol. 270, *Computational Star Formation*, Alves J., Elmegreen B. G., Girart J. M., Trimble V., eds., pp. 255–262
- Benjamin R. A. et al., 2003, *Publications of the Astronomical Society of the Pacific*, 115, 953
- Cazzolato F., Pineault S., 2005, *AJ*, 129, 2731
- Chaisson E. J., 1976, in *Frontiers of Astrophysics*, Avrett E. H., ed., pp. 259–351
- Chen B., Figueras F., Torra J., Jordi C., Luri X., Galadí-Enríquez D., 1999, *A&A*, 352, 459
- Comerón F. et al., 2002, *A&A*, 389, 874
- Cutri R. M. et al., 2003, *2MASS All Sky Catalog of point sources. The IRSA 2MASS All-Sky Point Source Catalog*, NASA/IPAC Infrared Science Archive. <http://irsa.ipac.caltech.edu/applications/Gator/>
- Dame T. M., Hartmann D., Thaddeus P., 2001, *ApJ*, 547, 792
- Davies B., Figer D. F., Kudritzki R.-P., MacKenty J., Najarro F., Herrero A., 2007, *ApJ*, 671, 781
- Davies B., Figer D. F., Law C. J., Kudritzki R.-P., Najarro F., Herrero A., MacKenty J. W., 2008, *ApJ*, 676, 1016
- Dempsey J. T., Thomas H. S., Currie M. J., 2013, *ApJS*, 209, 8
- Dickman R. L., 1978, *ApJS*, 37, 407
- Dorda R., Negueruela I., González-Fernández C., Marco A., 2016, in *Astronomical Society of the Pacific Conference Series*, Vol. 507, *Multi-Object Spectroscopy in the Next Decade: Big Questions, Large Surveys, and Wide Fields*, Skillen I., Barcells M., Trager S., eds., p. 165
- Draine B. T. et al., 2007, *ApJ*, 663, 866
- Drilling J. S., Landolt A. U., 2000, *Normal Stars*, Cox A. N., ed., p. 381
- Egan M. P., Price S. D., Kraemer K. E., 2003, in *Bulletin of the American Astronomical Society*, Vol. 35, *American Astronomical Society Meeting Abstracts*, p. 1301
- Ekström S. et al., 2012, *A&A*, 537, A146
- Ekström S., Georgy C., Meynet G., Groh J., Granada A., 2013, in *EAS Publications Series*, Vol. 60, *EAS Publications Series*, Kervella P., Le Bertre T., Perrin G., eds., pp. 31–41
- Elmegreen B. G., Lada C. J., 1977, *ApJ*, 214, 725
- Fich M., Blitz L., Stark A. A., 1989, *ApJ*, 342, 272
- Figer D. F., MacKenty J. W., Robberto M., Smith K., Najarro F., Kudritzki R. P., Herrero A., 2006, *ApJ*, 643, 1166
- Glenn J. et al., 2003, in *Millimeter and Submillimeter Detectors for Astronomy*, Phillips T. G., Zmuidzinas J., eds., Vol. 4855, pp. 30–40
- Griffin M. J. et al., 2010, *A&A*, 518, L3
- Gutermuth R. A., Megeath S. T., Myers P. C., Allen L. E., Pipher J. L., Fazio G. G., 2009, *ApJS*, 184, 18
- Helfand D. J., Becker R. H., White R. L., Fallon A., Tuttle S., 2006, *AJ*, 131, 2525
- Higuchi A. E., Kurono Y., Naoi T., Saito M., Mauersberger R., Kawabe R., 2013, *ApJ*, 765, 101
- Hildebrand R. H., 1983, *Quarterly Journal of the Royal Astronomical Society*, 24, 267
- Hollenbach D. J., Tielens A. G. G. M., 1997, *Annual Review of Astronomy & Astrophysics*, 35, 179
- Jackson J. M. et al., 2006, *ApJS*, 163, 145
- Kauffmann J., Pillai T., 2010, *ApJ*, 723, L7
- Koenig X. P., Leisawitz D. T., Benford D. J., Rebull L. M., Padgett D. L., Assef R. J., 2012, *ApJ*, 744, 130
- Kos J. et al., 2014, *Science*, 345, 791
- Lefloch B., Lazareff B., 1994, *A&A*, 289, 559
- Levesque E. M., Massey P., Olsen K. A. G., Plez B., Josselin E., Maeder A., Meynet G., 2005, *ApJ*, 628, 973
- Lockman F. J., Pisano D. J., Howard G. J., 1996, *ApJ*, 472, 173
- Lumsden S. L., Hoare M. G., Oudmaijer R. D., Richards D., 2002, *MNRAS*, 336, 621
- Martins F., Plez B., 2006, *A&A*, 457, 637
- Martins F., Schaerer D., Hillier D. J., 2005, *A&A*, 436, 1049
- Mauerhan J. C., Van Dyk S. D., Morris P. W., 2011, *AJ*, 142, 40
- Mezger P. G., Henderson A. P., 1967, *ApJ*, 147, 471
- Molinari S. et al., 2010, *Publications of the Astronomical Society of the Pacific*, 122, 314
- Negueruela I., Marco A., González-Fernández C., Jiménez-Esteban F., Clark J. S., Garcia M., Solano E., 2012, *A&A*, 547, A15
- Oka T., Onodera Y., Nagai M., Tanaka K., Matsumura S., Kamegai K., 2012, *ApJS*, 201, 14
- Ossenkopf V., Henning T., 1994, *A&A*, 291, 943
- Poglitsch A. et al., 2010, *A&A*, 518, L2
- Quiroza C., Rood R. T., Balser D. S., Bania T. M., 2006a, *ApJS*, 165, 338
- Quiroza C., Rood R. T., Bania T. M., Balser D. S., Maciel W. J., 2006b, *ApJ*, 653, 1226
- Reynoso E. M., Cichowolski S., Walsh A. J., 2017, *MNRAS*, 464, 3029
- Rieke G. H., Lebofsky M. J., 1985, *ApJ*, 288, 618
- Rieke G. H. et al., 2004, *ApJS*, 154, 25
- Schlafly E. F., Finkbeiner D. P., 2011, *ApJ*, 737, 103
- Schnee S. L., Ridge N. A., Goodman A. A., Li J. G., 2005, *ApJ*, 634, 442
- Sewilo M., Watson C., Araya E., Churchwell E., Hofner P., Kurtz S., 2004, *ApJS*, 154, 553
- Shirley Y. L. et al., 2013, *ApJS*, 209, 2
- Stil J. M. et al., 2006, *AJ*, 132, 1158
- Strong A. W., Mattox J. R., 1996, *A&A*, 308, L21
- Tokunaga A. T., 2000, *Infrared Astronomy*, Cox A. N., ed., p. 143
- Weaver R., McCray R., Castor J., Shapiro P., Moore R., 1977, *ApJ*, 218, 377
- Werner M. W. et al., 2004, *ApJS*, 154, 1
- Whittet D. C. B., ed., 2003, *Dust in the galactic environment*
- Wright E. L. et al., 2010, *AJ*, 140, 1868
- Zinnecker H., Yorke H. W., 2007, *Annual Review of Astronomy & Astrophysics*, 45, 481